Dynamic Light Scattering studies of fluid microdynamics

-

Master thesis

-

Author: **Loïc Jacot Descombes**

-

In the group of and supervised by: **Prof. Oleg Shpyrko, UCSD**

-

ETHZ Supervisor: **Prof. Bertram Batlogg**

-

March 26, 2009

Eidgenössische Technische Hochschule Zürich
Swiss Federal Institute of Technology Zurich

University of California
San Diego

Contents

Preface

This report summarizes a research project that I pursued within the framework of a Master Thesis of the "ETHZ" *(Eidgenössische Technische Hochschule, Zürich)*, internationally known as the *Swiss Federal Institute of Technology, Zürich* under the academic supervision of Professor Bertram Batlogg. I had the opportunity to do this research at the "UCSD" *(University of California, San Diego)* in the group and supervised by Professor Oleg Shpyrko.

Doing my Master in Physics, at the ETHZ, with an orientation in applied solid state physics. This master thesis offered me the possibility to deepen my knowledge, in one specific field, with a research project of four months. Since the internationality of the research in science is very important nowadays, , I decided to pursue this project abroad. I got in touch with Prof. Oleg Shpyrko, who offered me the opportunity to join his group.

Even though I spent long hours working in the lab, I also very much enjoyed life in Southern California. People being extremely curious and very friendly with foreigners, and the wonderful weather of this region offer an extremely comfortable situation for the nice city of San Diego.

Acknowledgements

I really would like to thank all people who gave me the possibility to pursue this research experience. First of all, I would like to express my sincere gratitude to Prof. Oleg Shpyrko, who offered me the opportunity to pursue this project in his group. I also want to thank him, as well as Yeling Dai, for the supervision and the precious help during this work. Their presence gave me the possibility to carry on these researches. I also would like to thank Dr. Jioty Mohanti for his very friendly help during the project, as well as the four undergraduate students, Andrew McLeod, Michael Folkerts, Sarah Garcia and Kevin Duggento who spent time with the group and helped the project at various stages. I thank Alberto Schena from the group of Prof. Yitzhak Tor for his samples. Of course, I also thank the Prof. Sunil Sinha and his entire research group for the very nice and helpful exchanges that we had between both groups, and specifically Yicong Ma for her help during the alignment of the optical setup.

Finally, I would like to express my very sincere gratitude to Prof. Bertram Batlogg, who encouraged me to organize this project abroad and kindly accepted to be my ETHZ supervisor.

Abstract

In this work I establish the required steps for studies of micro- and nano- particle diffusion, both in the bulk and in confined geometries. I will discuss a variety of technical and scientific issues related to light and in some cases x-ray scattering, and highlight relative advantages and disadvantages of several experimental approaches we pursued. I will demonstrate that the combination of Dynamic Light Scattering (DLS) performed with visible light and its x-ray counterpart, X-ray Photon Correlation Spectroscopy (XPCS) allows to study diffusion of particle, particle dimensions and diffusion lengths (or, inversely, scattering wavevectors) ranging over 3 orders of magnitude, and timescales ranging over more than 9 orders of magnitude. Focusing primarily on DLS experiments, I will discuss important experimental details, such as homodyne vs. heterodyne methods, importance of alignment, complications arising from multiple scattering, particle polydispersity, etc. The understanding of how these details may affect the outcome of the DLS measurements turned out to be crucial to successful application of DLS to particles with sizes ranging from micron-scale down to nanometer-scale.

I will also discuss the multi-speckle DLS that was performed using the multi-pixel detector (CCD camera). We have applied traditional intensity correlation method, as well as a novel approach of speckle visibility spectroscopy, both highly useful in studying time varying (non-equilibrium) dynamics.

1 Introduction

The development of micro and nano systems is nowadays a very important focus of applied physics. Microscale and nanoscale systems find applications in biology, chemistry, medicine and other fields of science and technology. Engineering performed in areas of mechanics, electronics and fluidics has to deal with various features at very small scales. In the case of fluidics, a better understanding of the diffusion within the confinement is one of the important requirements for the development of micro- or nano-fluidic systems. For example, the mixing rate of two flowing solutions depends on their diffusion. Other features that take a high importance at the micro- and nano- scale are surface tension and surface area to volume ratio. [1]

The development of micro or and nano scale devices has many potential applications in biochemistry and biomedical sciences. Some of the commercial applications of the MEMS (Microelectromechanical Systems) involve a large range of sensors, like pressure sensors, chemosensors, biosensors, to name just a few. Bio-MEMS are also used in the development of lab-on-a-chip applications, which are very small devices that can accomplish several of the numerous functions done by a standard chemical lab. The minuscule scale of those systems has various advantages, such as the low cost, the ability of in-situ monitoring of biological or medical parameters, fast real-time analysis and many others. A better understanding of micro and nanoscale fluidics will offer new possibilities in various applications, such as protein folding, crystallization etc. [2]

In our research project we aimed to study diffusion of simple particles first laying the groundword for understanding the diffusion of more complex particles, like biological proteins. The idea was to compare the diffusion coefficient for bulk and confined solutions. Starting with a suspension of mircoparticles, we moved then to suspensions of nanoparticles, and later to nanoparticles in nanopores [3]. For those studies, we used the information provided by the Dynamic Light Scattering. As a comparison, we also include in our project some X-ray Photon Correlation Spectroscopy (XPCS) data analysis of previous experiments. [4]

This thesis will describe experimental approaches to study diffusion of nanoparticles (6-50 nm in diameter) confined in 100 and 200 nm diameter pores, as well as larger scale particles (up to about 1 micron diameter). We will discuss experimental challenges in studies of nanometer-sized particles as well as relative advantages and disadvantages of various speckle detection schemes.

2 Background

2.1 Brownian motion

The Brownian motion is a ubiquitous interesting feature of a colloidal solution: particles immersed in a solvent, such as water, undergo a random motion. This diffusive motion is called the Brownian motion and was first discovered in 1827 by Robert Brown [5]. Theory of this phenomena was developed by Albert Einstein and Marian Smoluchowski after the kinetic theory formulation from James Clerk Maxwell and Ludwig Boltzmann [6, 7]. Several famous physicists studied Brownian motion, and have established both theoretically and experimentally that the rate of the particle motion depends, among others, on the particle size, the viscosity of the solution and the temperature.

2.2 Diffusion

The thermal agitation of the solvent molecules induces a random walk of the particles in suspension. Introducing the root mean displacement ($< X >$), the time for one step (Δt), the position after n steps (X_n) and the length of one step (ΔX), the position after n steps can be expressed by:

$$X_n = X_{n-1} + \Delta X \quad implying \quad < X_n^2 >= n\ \Delta X^2 \tag{1}$$

Where the number of steps at a time t is given by $n = t/\Delta t$, which implies:

$$< X^2 > \sim\ t\ D \tag{2}$$

The minimum root mean square displacement can be related to scattering wavevector transfer q:

$$< X^2 > \geq\ \left(\frac{2\pi}{q}\right)^2 \tag{3}$$

Giving equations (20) and (21).

The diffusion coefficient, D, in the case of spherical particles (Stockes friction), is given by the following Einstein relation:

$$D = \frac{k_B T}{6\pi\eta r} \tag{4}$$

Where r is the hydrodynamic radius of the particles in suspension, k_B is the Boltzmann constant, η is the viscosity of the solvent and T is the temperature. The hydrodynamic radius represents the diameter of a sphere that has the same translational diffusion coefficient as the particle being studied. The latter takes into account the particle size, the various surface structures and other quantities which may affect the particle diffusion (an example is given in Figure 10).

2.3 Light scattering experiments

2.3.1 Description

As we will later demonstrate, the coherent light scattering techniques can be applied over a wide range of spectrum - from visible light (wavelengths on the order of 400-700 nm) to hard x-rays (wavelengths on the order of 0.1 nm). This chapter will focus on scattering experiments performed with visible light.

Since the invention of lasers over 50 years ago, light scattering has found many applications in areas of science and technology. For example, it is a very powerful method for characterizing macromolecules. The coherence of the light source offers the possibility for studying the dynamics in heterogeneous systems.

Figure 1 shows a scheme of light being scattered by a colloidal solution.

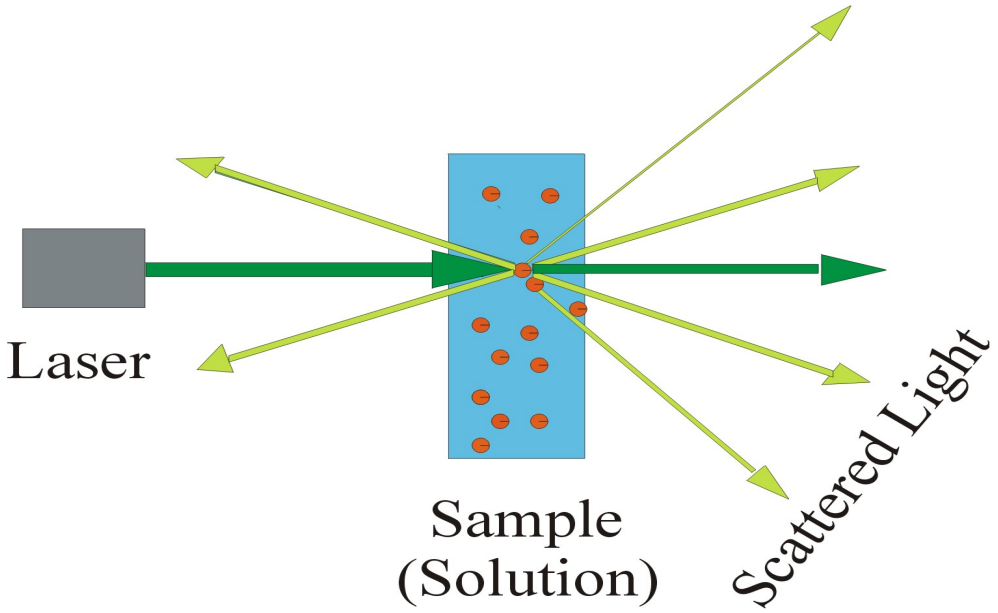

Figure 1: *Scattering geometry showing transmitted direct beam from the laser (dark green) and the light quasi-elastically scattered by the colloidal particles (light green).*

Our interpretation of light scattering in this thesis will be performed using the following three assumptions: (1) Incident and scattered waves have the same wavelength (quasi-elastic scattering approximation). (2) The independence of the particles, meaning that each particle serves as a separate and well-defined scattering point. (3) Each photon scatters no more than once - that is multiple scattering effects can be neglected. As we will see later, the multiple scattering approximation may not always be applicable for our experiments.

The basic physical mechanism of light scattering is that the electromagnetic field from the

incident wave induces dipole moments in the scatters. The dipoles oscillate at the frequency of the applied field, and therefore, radiate the scattered field in all directions. The scattered field at any location is the coherent superposition of all radiated wavelets. [8]

2.3.2 Different kinds of light scattering

Several light scattering methods have been developed. Three common ones are Static Light Scattering, Surface Light Scattering and Dynamic Light Scattering (DLS).

The static light scattering is typically used to calculate the Radius of gyration (R_g) for the molecule or particle, which can be used to calculate the average molecular weight. The basic idea is to measure the intensity as a function of scattering angle, or wavevector.

Surface Light Scattering consists of the analyze of the structure and the fluctuations of a surface by a scattered light from the interface between the liquid and the gaseous phase. On liquid surfaces, the surface waves, due to particle thermal motion, are quantized in *Ripplons*. The latter studies allow the determination of the viscosity or of the surface tension, to quote few of the possible applications. [9]

2.4 Detectors and Correlators

Typically, the detection setup is composed of the detector (typically a Photomultiplier Tube, a photodiode or a Charge Coupled Device), the correlator (hardware or software) and the computer. The signal measured by the detector is the intensity of the light. The detector measures the photocount during each sampling time. The signal is converted to the form of dc current pulses and is transmitted to the correlator. The electronic signal is proportional to the intensity, via a scaling constant related to the quantum efficiency of the photocathode. In order to calculate the intensity autocorrelation function, the correlator compares the intensity at two different times separated by the delay time. This calculation is averaged for different pairs of intensity measurements separated by the same delay time, and then the entire calculation is performed for different delay times. [10]

Mathematically, the photocount correlation function is given by:

$$C(t) \equiv \langle n(t) \cdot n(0) \rangle \tag{5}$$

where n(t) is the number of photons arriving in the time interval between t and t + δ t. [11]

2.4.1 The Photo Multiplier Tube

A Photomultiplier Tube (PMT) is composed of a scintillator, where an incident photon is converted into an electron via photoelectric effect. This electric signal is magnified many-fold by accelerating electrons and generating secondary electrons via collisions of electrons

with dynodes. The PMT is connected to a correlator, in our case, a computer board, which correlates the measured intensity. The correlators that are commercially available can compute the intensity correlation over a large range of delay times, typically from 10 ns to 100 s [12]. The correlator can calculate either the cross correlation function of two different signals (A and B) or the autocorrelation function of a single signal.

The photomultiplied detectors can be interpreted as 0D detectors, or point detector, because they provide a single channel of the measured intensity at a single detection point, becoming effectively a one-pixel detector. Thus, the correlation function is time averaged, process which requires a long time for precise results. The advantages of the PMT detector are the high dynamic range, fast readout and short dead time, allowing measurements of very rapid intensity fluctuations, up to frequencies of 1 GHz (timescale as short as 1 ns).

2.4.2 The CCD camera

The CCD (Charge Coupled Device) camera is an array detector which is composed of arrays of semiconducting charge "buckets" surrounded by an electric condensator corresponding to the pixels of the camera. It is thus possible to have a lot of pixels (with typical dimensions on the order of 10-100 microns) next to each other, which makes a 1D (a line) or a 2D (an area) detector. The advantage of those detectors over the one pixel detectors such as PMTs, is their ability to measure the scattered light intensity from several pixels at the same time. On other hand, the multiple-pixel detectors often suffer from slow readout rates, which does not allow the study of very fast dynamics. Nevertheless, in some situations, CCDs can be very useful and also allows the speckle size measurement [13], as will be demonstrated in section 2.5, 2.6 and 4.8.

2.5 Dynamic light scattering

Dynamic Light Scattering (DLS), also called Photon Correlation Spectroscopy (PCS) or Quasi-Elastic Light Scattering (QELS) is a method which is widely used in applied physics, chemistry and biology. As a non invasive technique, it has several very useful applications such as the measurements of the transport and thermophysical properties of fluids, particle sizing or protein folding studies. This technique has undergone major improvements during the past ten years, with many significant variations from the initials setup being developed.

The procedure of Dynamic Light Scattering experiment is to measure the intensity fluctuations of the scattered light over time. Those fluctuations are typically due to the relative motion of the scatterers, for example the Brownian motion of particles in suspension or the vibrations of a membrane. It is then possible to correlate this intensity measurement either with another one (cross correlation) or with itself (autocorrelation). The sample and the detector are mounted on a goniometer, which allows for measurements of scattered intensity and

its correlation functions as a function of scattering angle.

2.5.1 Measured intensity

1. *Angle dependence*

As mentioned previously, the detector measures the intensity of the incident light, which is an amount of photons per unit of time. For convenience, in the following calculations, I will consider the electric field of the light, with intensity proportional to the square of the electric field amplitude. While a complete description will not be given here, more details can be found in [14].

Starting with the real part of the electric field of the incident light, in the z direction:

$$E_Z = E_{Z0} \cdot \cos(k_0 y - \omega_0 t) \tag{6}$$

Where χ is the angle between the z axis and the observer direction, k_0 is the wavenumber, c is the speed of light, ϵ_0 is the permittivity of free space, ω_0 is the laser frequency and R is the distance between the scatterer and the observer. Introducing the polarizability, p, which gives the dipole magnitude induced by the light, we can express the scattered electric field:

$$E_S = \frac{\omega_0 p \sin(\chi)}{(4\pi\epsilon_0)c^2 R} \tag{7}$$

Since the fluctuations of the electric field are much smaller than the required time for the measurements, we obtain the scattered intensity by:

$$I_S = c\epsilon_0 \left[\frac{-\omega_0^4 \sin^2(\chi)}{(4\pi\epsilon_0)^2 c^4 R^2}\right] \tag{8}$$

and

$$\frac{I_S}{I_i} = \frac{\omega_0^4 \cdot \sin^2(\chi)}{(4\pi\epsilon_0)^2 c^4 R^2} = \frac{16\pi^4 \alpha^2 \sin^2(\chi)}{(4\pi\epsilon_0)^2 \lambda_0^4 R^2} \tag{9}$$

The incident light being polarized along the z direction (vertically in our case) and in the Rayleigh limit, we obtain the following, which gives the angular dependence (expressed in cgs units):

$$\frac{I_S}{I_i} = \frac{8\pi^4 \alpha^2}{\lambda_0^4 R^2}(1 + \cos^2(\theta)) \tag{10}$$

Thus, we can expect that the intensity is much higher for small angle and backscattering, than at 90°, where it should be minimum. We have also the concentration dependence that could be taken into account. The link between the cycle average intensity and the electric field is given by: [14]

$$I = EE^* = |E|^2 \tag{11}$$

2. *Particle size dependence*

One point which will take importance in the following is the dependence of the scattered intensity in the particle cross section, which expresses the amount of light scattered from the particle and is related to the size, see eq. (13). For a monochromatic incident light, the transition between the Rayleigh and the Mie scattering regime can be expressed using the following ratio.

$$x = \frac{2\pi r n}{\lambda} \tag{12}$$

We define r as the radius of the particle, n as the medium refractive index and λ as the light wavelength. If $x << 1$, we are in the Rayleigh regime (particles small compared to light wavelength) and if x is comparable or bigger than 1 we are in the Mie regime (particles of similar or greater size compared to λ). In the Rayleigh regime, the intensity of the scattered light is inversely proportional to the wavelength at the power of four and of three in the Mie regime.

In the case of the Rayleigh regime, the intensity of the light scattered from a single particle is given by:

$$I = I_0 \left(\frac{1 + \cos^2(\theta)}{2R^2} \right) \left(\frac{2\pi}{\lambda} \right)^4 \left(\frac{n^2 - 1}{n^2 + 2} \right)^2 \left(\frac{d}{2} \right)^6 \tag{13}$$

This relation shows that the scattered intensity is strongly dependent on the particle size. The scattering from 10 nm particles is 10^6 (a million!) times weaker than scattering from 100 nm particles.

The previous discussion could also include the concentration dependence. In the case of spherical particles, the scattering by a sphere was solved, and is known as the Mie solution. This solution is exact if the particle is spherical for any radius and refractive index. The Rayleigh scattering fails for particle sizes on the order of, or larger than the wavelength.

2.5.2 The Correlation

I will briefly show how it is possible to calculate a correlation function from the signal which is measured at the detector. The detector measures the intensity of the light vs the time, as explained in section 2.4 and 2.5. To obtain the autocorrelation of this intensity, the correlator compares the intensity at the time τ_0 and the intensity measured after different delay times. As we can see in the Figure 2, the closer are the delay time to τ_0, the closer are the values of the intensity measured at those times. Thus, the correlation for sufficiently short delay times is expected to be relatively high. With increasing the delay time, the correlation will be lower on average. We see that for a long delay (such as the one shown with blue line in the Figure 2), the pair of measured intensity values become completely uncorrelated with

each other. Instead, for short delay times (for example measurements taken at points p, q, r in green in the Figure 2) the value of the intensity remains similar. The Correlation function is built point per point by comparing the intensity at the time τ_0 with the one after a delay time that increases. With this process, we get the correlation of the intensity of our signal vs the delay time. The correlation function expressed in Figure 2 will be normalized.

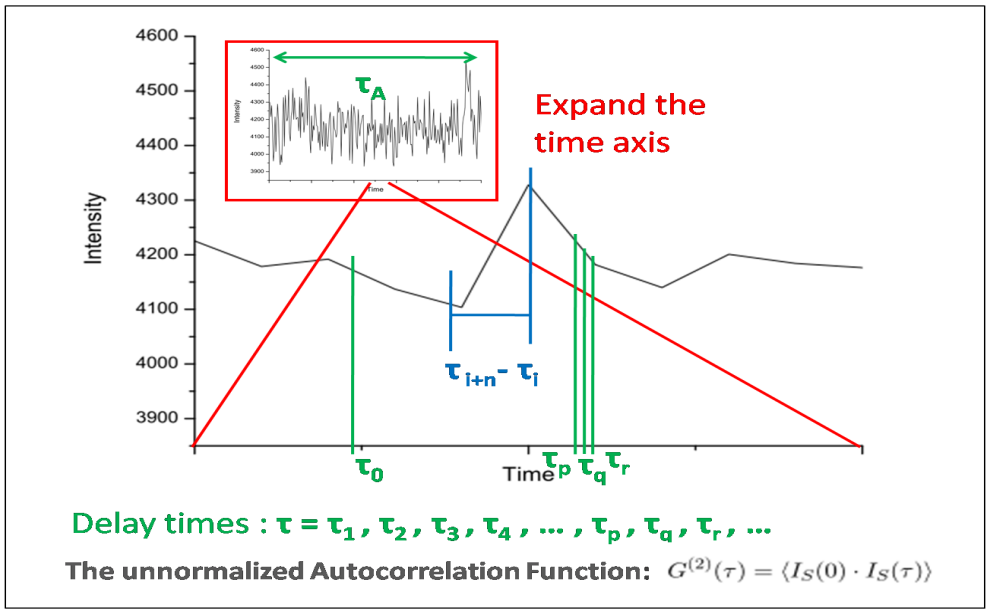

Figure 2: *Autocorrelation of the measured signal intensity from a "point" (0D) detector. It is shown that for short delay times, the correlation is high, but decreases for longer delays*

The use of area or line detectors simply offers an opportunity of many measurements of the correlation function done in parallel, with each pixel on the detector becoming its own detector. The resulting correlation can be averaged together if the q vector is the same, or, if pixels are at sufficiently different values of q, they can provide q-dependence of the autocorrelation function. This is the process which is used for the x-ray data analysis that we will discuss in section 4.8.

The scheme from Figure 3 shows how to compute the autocorrelation function in the case of a 2D detector. The result is the temporal autocorrelation for each of the pixels, which provides us with wavevector q dependence. We can get significantly improve counting statistics by averaging several pixels, or partitions over similar q values.

2.5.3 Correlation and Autocorrrelation functions

As we discussed in section 2.4, the hardware correlator board provides us the cross correlation function (CCF) or the autocorrelation function (ACF). The correlation is calculated

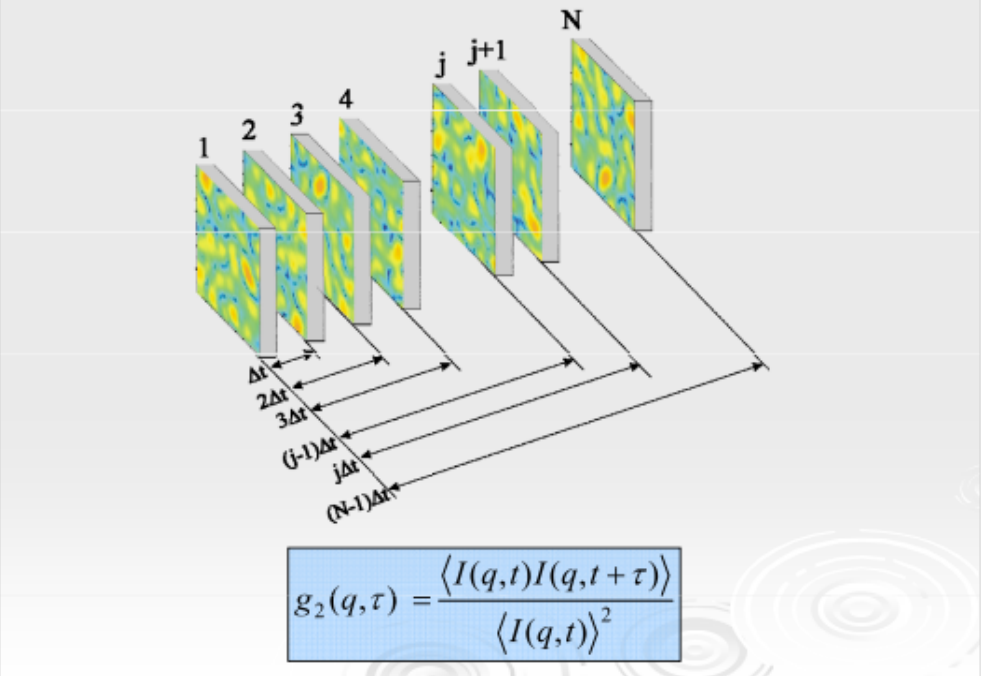

Figure 3: *Autocorrelation of the intensity from an area detector, adapted from [15] The frames can be correlated, as well as the pixels of one frame.*

between the intensity at two different times t_1 and t_2. We define this time delay as $\tau = t_2$ - t_1.

The expression of the first order ACF is

$$G^{(1)}(\tau) = \langle E_S^*(t) \cdot E_S(t+\tau) \rangle \tag{14}$$

and can also be written as

$$G^{(1)}(\tau) = \langle E_S^*(0) \cdot E_S(\tau) \rangle \tag{15}$$

because $E_S(t)$ is a stationary random variable, and its properties are independent of the time origin. We can also give the second order ACF.

$$G^{(2)}(\tau) = \langle I_S(0) \cdot I_S(\tau) \rangle \tag{16}$$

We can now normalize this value by the square of the average intensity, to arrive at the dimensionless correlation function:

$$g^{(2)}(\tau) = \frac{\langle I_S(t) \cdot I_S(t+\tau) \rangle_t}{\langle I_S(t) \rangle^2} \tag{17}$$

We consider now $E_S(t)$ to be a Gaussian random variable of a normalized ACF and we introduce the parameter β, which is a correction factor (also known as Siegert coefficient) introduced to take into account the geometry and alignment of the laser beam. This factor is proportional to the inverse of the speckle number detected. We can then use the Siegert relation:

$$g^{(2)}(\tau) = 1 + \beta[g^{(1)}(\tau)]^2 \tag{18}$$

A simple approach for further calculation is to consider the first order ACF as a summation of exponentials, we introduce the decay rate, Γ.

$$g^{(1)}(\tau) = \sum G_i(\Gamma i) \exp(-\Gamma i \tau) = \int G_i(\Gamma) \exp(-\Gamma \tau) d\Gamma \tag{19}$$

Finally, using the cumulant method, introducing D (diffusion coefficient), we can express the average decay (particle diffusion) rate as:

$$\Gamma = q^2 D \tag{20}$$

Which is defined by:

$$\Gamma = \frac{1}{\tau} \tag{21}$$

Where τ is the characteristic time, in other words, the delay time in the correlation function at which occurs the decay.

The vector q is the momentum transfer, $\overrightarrow{q} = \overrightarrow{k_i}$ - $\overrightarrow{k_s}$, the difference between $\overrightarrow{k_i}$ (incident) and $\overrightarrow{k_s}$ (scattered) wavevectors, and is given by:

$$q = \frac{4\pi n}{\lambda} \sin(\frac{\theta}{2}) \tag{22}$$

Where λ is the wavelength of the laser, n is the refractive index of the solvent and θ is the angle between k_i and k_s. [11, 14]

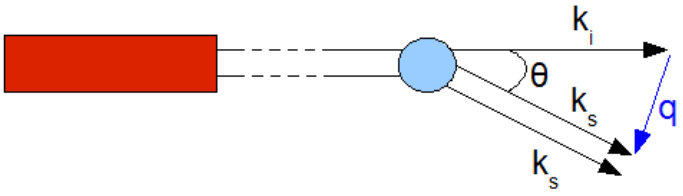

Figure 4: *Paths of incident and scattered light*

The signal is then given by time averaging, or in the case of ergodicity, we can also average it with the ensemble. The calculation of the correlation for different delay times yields the time at which the coherence decays. We get the (auto) correlation function versus the time delay. As an example, this ACF can be the correlation length of a Brownian suspension.

2.5.4 Coherence of light

The previous chapter introduced the Correlation and the Autocorrelation explicitly assuming that the light source is coherent. I will now briefly speak about this requirement.

Two waves are coherent if they have a constant phase relationship. The coherence of light can be separated into longitudinal and transversal. We can express the longitudinal (23) and the transverse coherence lengths (24) as:

$$l_l \approx \frac{\lambda^2}{2\delta\lambda} \tag{23}$$

$$l_t = \frac{\lambda R_s}{2d_s} \tag{24}$$

Where λ is the wavelength, R_s is the distance between the source and the observation, d_s is the source diameter and $\delta\lambda/\lambda$ is the relative bandwidth of the source. The correlation of two waves give us their coherence. Doing the latter with only one source will yields its mutual coherence. The mutual coherence can be expressed by:

$$\Gamma_{1,2} =< \vec{E}^*(r_1, t_1)\vec{E}(r_2, t_2) >_t \tag{25}$$

A source is told to be coherent if there is a non-zero statistical correlation between $\vec{E}(r_1, t_1)$ and $\vec{E}(r_2, t_2)$. [16]

As a consequence we see that if we want to measure a lost of coherence in our (auto)correlation function, the source needs to be coherent. In the Figure 5 we have a representation of a coherent and of an incoherent light source.

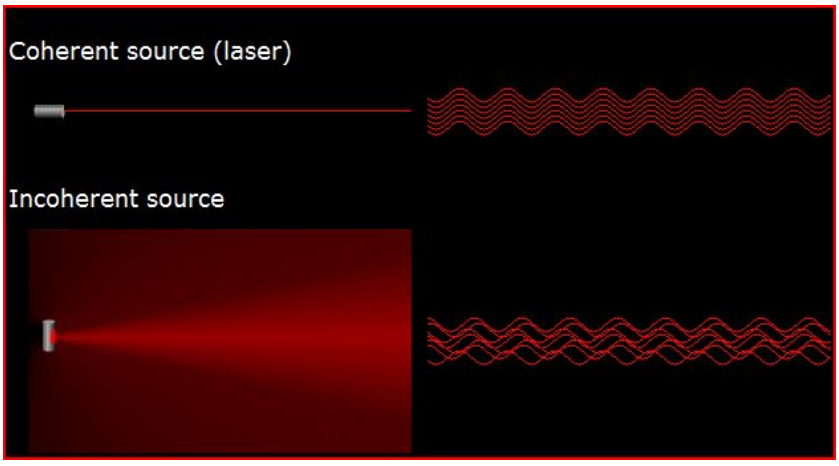

Figure 5: *A schematic illustration of the wavefronts produced by the coherent light source (such as laser) and incoherent light source (such as incandescent light bulb).*

2.5.5 Speckle size

When illuminated with coherent wavefront, the interference between randomly positioned scatterers gives rise to a complex interference pattern consisting of areas of high and low light intensity - so called "speckle" pattern. The size of the speckle is defined by the longest interference path between the two scatterers located far apart. This distance D is typically related to the diameter of the laser beam, the transverse coherence length, or the transverse

dimensions of the sample, whichever is the smallest. The speckle size is given by the equation:

$$Speckle\ size = \frac{\lambda z}{D} \tag{26}$$

Where λ is the laser wavelength, z the sample-detector distance and D is the laser beam cross section diameter. The coherence area on the detector depends on the focus of the laser, in the sense that the more focused is the laser beam on the sample, the larger is the coherence area (the speckles).

The use of a CCD camera allows the analysis of speckle size. The speckle size is usually not equal to the CCD camera pixel size. The small speckles, on the detector, come from large halo of multiple scattered photons and the large speckles come from a small region of single scattering. If the speckle size is smaller than pixel size, the effective speckle contrast (given by Siegert coefficient) will be reduced due to averaging over several nearby speckles. If, however, the speckle size is greated than the pixel size, it is possible to combine (or "bin") several pixels together and to approximate their intensity by an integral over all of them. This is called the *binning method*. It is then possible to consider not only a single pixel, but a bunch of pixels together, which is called a *meta-pixel* or a *bin*. Thus, it is possible to correlate pixels coming from the same coherence area (speckle) or from different ones.

This method allows a multiple scattering suppression scheme using the cross-correlation between two different pixels (meta-pixels). The pixels that are correlated can belong either to the same coherence area or to two different coherence areas, or to a superposition of both. In the latter case, the measured intensity will be correlated only due to the large speckles, coming from single scattering. [13]

Typically an improvement in signal-to-noise in autocorrelation function is achieved via averaging over t in equation (17). This averaging can be justified only for equilibrium processes, so that the time constants associated with dynamics do not significantly vary over the duration of time t. I will now write about an interesting method based on the speckle visibility using a CCD camera allowing the time-varying (non-equilibrium) dynamics study. The idea is to calculate the intensity maximum and minimum (see eq. (27)) over all pixels at a given time (one line of an image provided from the CCD line detector). Then speckle visibility $f(\tau)$ is calculated for the average of the two first lines of the image; the second line corresponding to the measured intensity of the same pixels, but after a delay time τ. Since the averaging over many time-dependent intensity fluctuations produces similar average intensity values for all pixels, speckle visibility $f(\tau)$ reaches 0. The decay in $f(\tau)$ (eq. (27)) represents to the lost of coherence. The process is shown in the scheme in (Figure 16), and was introduced by [12]

$$f(\tau) = \frac{I_{max}(\tau) - I_{min}(\tau)}{I_{max}(\tau) + I_{min}(\tau)} \tag{27}$$

2.5.6 Multiple Scattering

Single scattering occurs when a radiation is scattered by one localized scatterer before being detected while multiple scattering occurs when detected light scatters more than once. In the latter case, depending on the scattering volume and the concentration, the photon mean free path is shorter than the scattering volume and the photon undergoes several interactions before to reach the detector. Thus, the angular dependence, requiring that the scattering occurs in the center of rotation, is lost. Multiple scattering becomes especially important for high concentration solutions. If multiple scattering is considerable, the measured correlation function deviates from its theoretical expectation and the decay occurs for shorter delay times. As a result, the measurements produce apparent dynamics that is faster than expected, which means, in the case of particle sizing, a smaller particle size than expected. Scientists found out several methods to reduce or suppress multiple scattering effects. One way is to connect the detector to an optical fiber and to introduce it directly inside the scattering volume which reduces the distance that the photon has to pass before reaching the detector [17]. Another possibility is to use digital camera detection scheme capable of discriminating the speckles arising from single and multiple scattering by their size, as explained in [13]. More detailed description of multiple scattering is given in [18].

2.6 Other experimental features

In this chapter, I will write about additional experimental properties: Homodyne or Heterodyne methods and the *Area* or *Point* detectors.

2.6.1 The Homodyne method

In the Homodyne method, the measured intensity comes only from the scattered light, ie, we don't measure any unscattered light. In the case $E_S(t)$, which is the summation of all $E_i(t)$ coming from different partition of the scattering volume, can be regarded as a Gaussian variable, it can be characterized by its first and second moments.

The term $|I_1(t)|$ is used to determine the baseline, which is the normalization term in the homodyne correlation function. It can be expressed:

$$I_1(t) = \sum a_i \cdot \exp(-t/\tau_i) \tag{28}$$

$$I_2(t) = \mid I_1(0) \mid^2 + \mid I_1(t) \mid^2 \tag{29}$$

$$I_2(t) = \sum a_i a_j \left[1 + \exp\left(-t\left(\frac{1}{\tau_i} + \frac{1}{\tau_j}\right)\right)\right] \tag{30}$$

In the case of a process which has only one relaxation time (one decay in the autocorrelation function), the relaxation time is $\tau/2$ instead of τ. [11]

2.6.2 The Heterodyne method

The idea of the Heterodyne method is to mix a portion of the unscattered light, called local oscillator, with the scattered light. Thus the measured intensity, in the detector, is composed of the scattered and of the unscattered light. The experimental setup for this method usually involves the separation of the laser light in two beams before the sample. One will be scattered in the sample and the other will not. The scattered and unscattered beams will be combined together after the sample. This method requires some additional devices than the Homodyne method but allows for example to have a very high local oscillator, which increases the total intensity of the signal. The autocorrelation function of the PMT output can be expressed as:

$$\langle i(0)i(t)\rangle = B\langle|E_{LO}(t) + E_S(t)|^2|E_{LO}(0) + E_S(0)|^2\rangle \tag{31}$$

Where, E_{LO} represents the local oscillator, E_S the scattered field, and B a proportionality constant.

Several approximation are possible, such as neglecting the fluctuations of the local oscillator, neglecting the second order of the scattered field, if $|E_{LO}(t)| >> |E_S(t)|$, or the statistical independence of the local oscillator and the scattered field. As a consequence, in the Heterodyne method, there are not as many exponentials as there are in Homodyne case. [11]

2.6.3 Point vs Area detectors

The accuracy of the ACF measured with a point detector will depend on the correlation average time over which the correlation for different delay times is averaged. One way to improve this accuracy without increasing the duration is to make spacial averages, instead of time averages. A spacial average of the ACF is done with two different pixels, with the same q. Thus, if we can measure a lot of different intensities, with different pixels, we will be able to improve the signal to noise ratio by averaging over many speckles within the same frame, rather than traditional way of averaging autocorrelation function over many time constants. The accuracy is therefore enhanced, without requiring for averaging over time. As a result, the use of CCD detectors in such multi-speckle detection scheme allows studies of time varying (non-equilibrium) dynamics. On the other hand, one of the disadvantages of the area detectors is the required acquisition time, which is usually much longer than for the point detectors. The consequence is that we cannot measure short delay times, we are thus restricted

to measurements of relatively slower dynamics.

As a consequence of the previous discussion, an interesting experiment is to combine a point detector with an area detector, in order to measure fast dynamics and simultaneously slow dynamics with high accuracy. Since the dynamics is q dependent, it is also possible to investigate dynamics at a wide range of lengthscales by changing the angle of measurement. [19]

2.7 X-ray Photon Correlation Spectroscopy (XPCS)

In this section I will discuss the X-ray Photon Correlation Spectroscopy (XPCS). XPCS is in many ways analogous to DLS, but as the name implies, carried out using x-ray photons, rather than visible light.

The use of x-ray photons as opposed to visible light has several key advantages:

1. The scattering wavevectors typically accessed with XPCS are 3-4 orders of magnitude greater than the ones typically used in DLS measurements, since the wavelength of x-rays is much shorter (7.35 keV hard x-rays used in XPCS measurements shown in section 4.8 correspond to λ=0.168 nm, much smaller than the red light λ=633 nm used in DLS). This allows access to much shorter diffusion lengths, on the order of just a few nanometers (comparable to relevant confinement length scales).

2. Hard x-rays scatter much more weakly from matter and as a direct result, they can easily penetrate through many opaque materials. This has two important consequences: multiple scattering processes can in most cases be safely neglected, and the amount of "parasitic" scattering from (thin) windows, dust, air and experimental components that x-ray beams pass through is typically much smaller than contributions from the samples.

3. X-ray scattering is proportional to the square of electron density, which means that scattering from high-z elements, such as gold (the metal commonly used for nanoparticle synthesis) will dominate scattering from soft materials, which are typically low-z (hydrocarbons) or the confinement matrix, which is aluminum oxide.

One of the key challenges in XPCS is the lack of x-ray sources with sufficiently high coherence (directly related to spectral brightness). As a consequence, XPCS was only made practical at third-generation undulator-based synchrotron sources, such as Advanced Photon Source, *Argonne National Laboratory*. Even at these brightest sources of x-ray radiation, the coherent content of the full x-ray beam is typically on the order of 0.01 %, meaning that a reasonable Siegert factor (on the order of 0.1 to 0.5) can be achieved only at the expense of a factor of 1,000 or more loss in photon flux, typically done via spatial filtering (pinhole) of the x-ray beam. Despite complexity and high cost associated with large synchrotron sources,

total photon flux per coherent mode at 1 mile circumference storage ring of Advanced Photon Source is lesser than the same figure of merit for a typical laser pointer. However, soon-to-be available fourth generation synchrotron sources, such as X-ray Free Electron Lasers and Energy Recovery Linacs will feature a nearly 100 % transverse coherent beams and will present a unique opportunity for XPCS and other coherent x-ray scattering techniques. [4, 20]

As a consequence of low coherent flux of currently available x-ray sources, and relatively weak scattering cross section for x-rays, the XPCS measurements are typically performed in multispeckle detection regime, using area CCD detectors to enhance the signal to noise ratio by measuring intensity fluctuations for many speckles simultaneously, as will be shown in the section 4.7.

2.8 Error estimation

In this chapter, I will briefly introduce some error sources and uncertainties which can occur in DLS measurements. For the autocorrelation function, we have two main sources (1 and 2):

1. *The Signal-to-Noise ratio*

An appropriate pinhole size of the detector optics will intensify the decay of the correlation function. The signal to noise depends on the quality (primarily coherence) of the light source. In order to improve signal to noise ratio for the measured signal, the detector optic includes a filter. In the case, one measures either the autocorrelation function of the photomultiplier tube, or its corresponding spectral density, the noise is composed by a shot noise and a thermal noise. In the following, I neglect the thermal noise.

The shot noise arises due to statistical fluctuations. It is important to take it into account in the situations in which the measured quantities (e.g. photon counts) are small. For large statistical samples, the Poisson statistic tends to the normal distribution, thus the Signal to noise ratio is proportional to $\sqrt{N}$ where N is the average number of photons detected in a given measurement.

In the case where the illuminated part of the photocathode is smaller than one coherence area, the signal to noise ratio for autocorrelation function term due to the shot noise is given by:

$$\frac{s}{n} = \frac{i_0}{e} = \frac{N\langle ic\rangle}{e} \tag{32}$$

Where i_0 is the total average photocount, e is the electronic charge, N is the number of coherence areas (speckles) and $\langle ic\rangle$ is the average current contribution of a coherence area.

2. *The infinite time average*

Another source of error is the finite time average. The longer is the time over which we average our correlations, the more accurate is our autocorrelation function. The finite time average error is given by:

$$\Delta C(t) = \pm(\frac{2\tau_C}{T})^{1/2}[1 - C(t)] \tag{33}$$

Where τ_C is the correlation time, $C(t)$ is the normalized correlation function and T is the averaging time. [11]

3. *The measurement uncertainties*

The measured quantities during the experiment have also some imprecision. In the calcu-

lation, we use the usual propagation error expressions. For a calculated quantity depending on n measured quantities, we can express:

$$\Delta G(x_1, ..., x_n) = \sqrt{\sum_{i=1}^{n} \frac{\partial G}{\partial x_i} \Delta x_i} \tag{34}$$

4. *The polydispersity*

I include the polydispersity in the discussion of errors, even though it is not an error source but a component of an experimental result. In fact, in the estimation of the particle size, the difference between the expected and the calculated (measured) values is often partially due to the polydispersity. The latter represents the relative variance $\left(\mu_2/\overline{\Gamma}^2\right)$, where μ_2 is the intensity-weighted variance of the diffusion coefficient. It is a measure of the decay rate distribution, $G(\Gamma)$. We can expect the cumulant analysis to work well for a polydisoersity $\leq$ 0.3. [21]

Sometimes, the polydispersity of our measurements is very high. In those cases, it mainly means that our sample contains particles, or compounds of various sizes. One of the major consequences is that the measurements don't fit with the expected value, even taking into account the imprecision error. Even though some of our particle size don't fit properly with the expectation, the correlation functions still have physical meaning..

5. *Imprecision source treatment in this thesis*

In my writing, I will introduce, in most results, the measurement imprecisions and the polydispersity. According to equation (33), *The infinite time average* is strongly dependent on the average time. In the graph shown in Figure 6, we can see that while the delay time is increasing, the average time being constant, *The infinite time average* imprecision is constant. Since it is often impractical to carry out long measurements, the uncertainties for long time delays are often very large. Nevertheless, our correlation functions are very representative. Thus, in order to avoid clutter, especially when showing multiple datasets, I didn't introduce the error bars in our results. Below, (Figure 6) I show a typical autocorrelation function with this imprecision in order to clarify the previous discussion.

In the results shown about particle sizing in the following chapters, the error on our estimation of the particle diameters and the one on the *Brookhaven's* diameter is done with the relation (34).

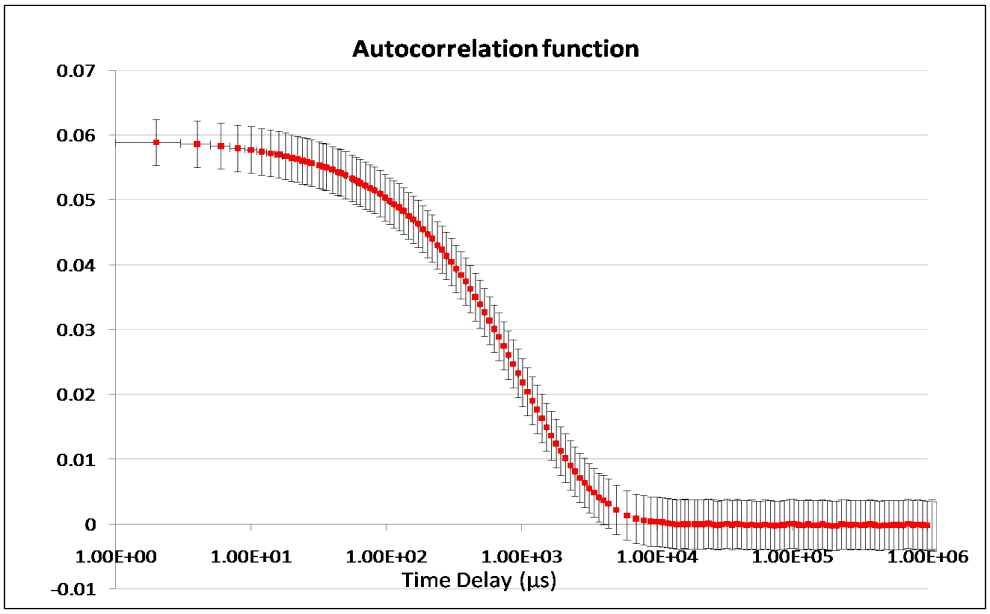

Figure 6: *Representation of the "Infinite Time Average" imprecision with one of our typical ACF (averaging time of 2 mins).*

3 Instrumentation

Before describing each device separately, I show in the following image, a scheme of our setup.

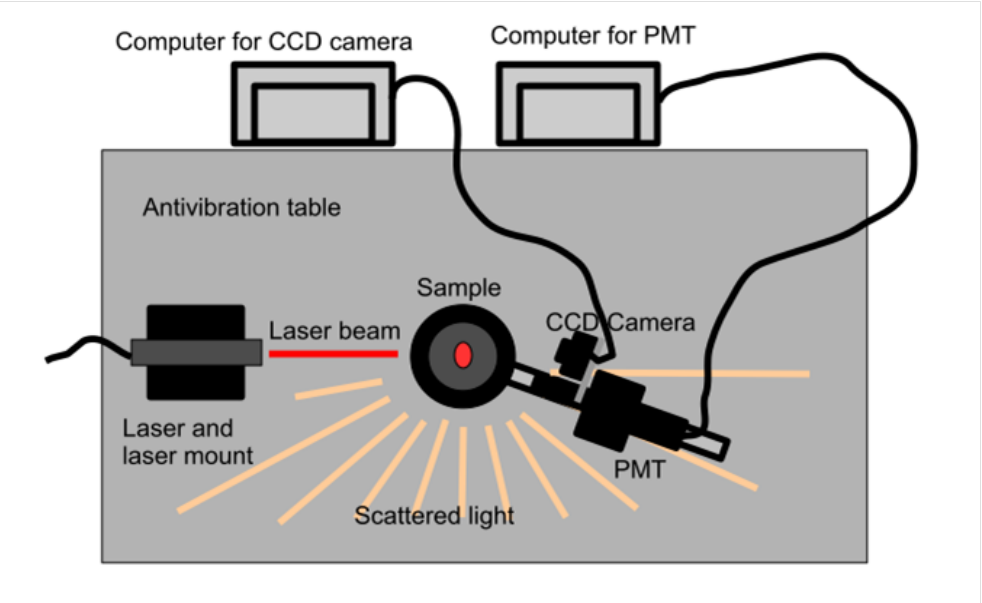

Figure 7: *Scheme of our Setup*

3.1 Dynamic light scattering setup

Our DLS setup is composed of the Goniomter , the Laser, the Detectors (the Photomultiplier and the CCD camera), the Antivibration table and the computers with the required softwares.

3.1.1 The Laser

We used a 5.0 mW power laser with a wavelength of 633 nm. It is provided from *Research Electro Optics, USA*. The beam is 1 - 2 mm wide. The laser is mounted on a metal rod, which is fixed on *Newport* stage allowing translational and height control. The clamp allows a 2 dimension rotation. These degrees of freedom (height, translation and rotation) were extremely convenient for the alignment of the laser beam to coincide with the center of rotation of the Goniometer.

3.1.2 The Goniometer

We have used BI-200SM Goniometer, Ver.2.0, from *Brookhaven Instruments Corporation*. It allows a 360 degree rotation. The scattering angle could be adjusted manually or with a

motor. The Goniometer includes a rail for mounting the detector.

3.1.3 Matching index

In order to avoid any substantial change in the index of refraction (and therefore reduce amount of scattering) close to the sample, the Goniometer was provided with an index matching cylindrical vat. The laser beam enters the vat through a polished flat area. The vat is to be filled with a matching index liquid, Decalin (Decahydronaphthalene (cis + trans) or bicyclo[4.4.0]decane), which has a refractive index between 1.469 and 1.481. To contain our solutions, we used Pyrex tubes, which have a refractive index very close to the one of Decalin. The Glasspyrex has a refractive index of 1.474. The refractive index of water is somewhat lower (1.333).

3.1.4 The PMT, the Correlator and the Software

The PMT and the correlator are also provided by *Brookhaven Instruments Corporation*. The detector optics, composed of a pinhole, a frequency filter, a slit and a lens, is mounted on the detector arm, immediately in front of the PMT. The correlator that we used was the BI-9000AT Digital Autocorrelator. It allows a minimum delay time of 25 ns, with a maximum count rate of 40 Mcps. The latter can make cross and auto correlation. There are three different working regimes, the Low, Mid and High speed regimes, depending on the delay time range in which we are interested. The maximum number of channel is 522. The dynamic range is over 10 decades.

Among the various information that can be calculated by using the Brookhaven Instruments analysis software, we are typically interested primarily in particle size, autocorrelation functions and related parameters. The *Poly* in the Figure 8 , inset (a), stands for *Polydispersity* and is a measure of the decay rate distribution. The latter can be obtained via a second order fit and gives the size distribution width. In the specific case of data shown in Figure 8, we see that the ACF has a contrast in the order of 5 %. We see that the software also gives the measured and the calculated baseline (M.Base and C.Base) which are used as a normalization factor for the ACF, see equation (17).

3.1.5 The CCD Camera, the Frame grabber and the Software

The CCD camera that we used comes from *Basler Vision Technologies*. The model name is *Sprint spL2048-140km*, and it is the version of 01.02.2004. It is a two line CCD, with 2048 pixels per line. Each pixel is 10 μm x 10 μm. The sensor is a Linear CMOS with Bayer color filter. The camera link clock speed is 40 MHz, or can also be setup at 80 MHz. The minimum line acquisition rate is 1 kHz and the maximum line rate is 70 kHz. To use the camera, we

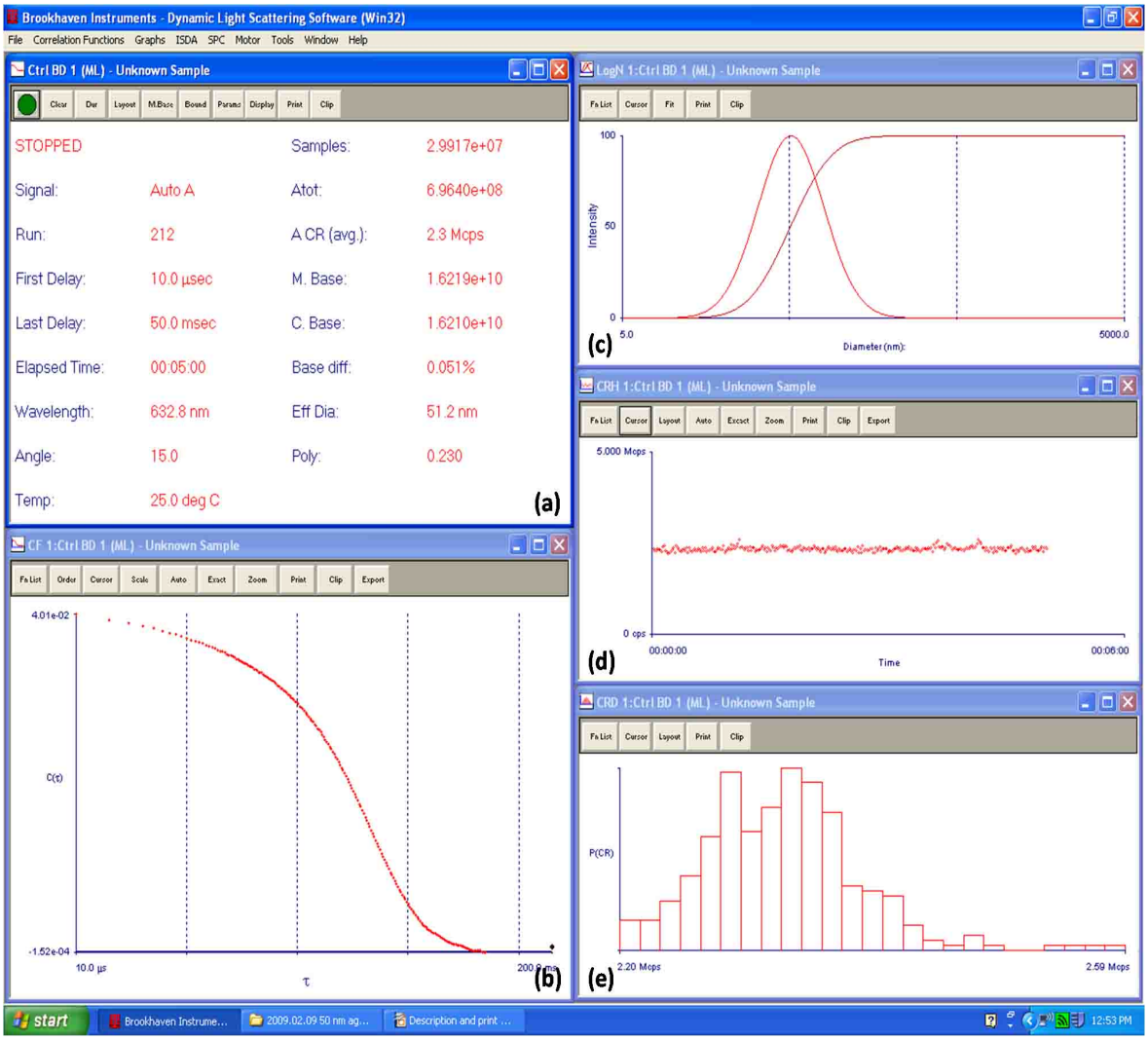

Figure 8: *An example of a print screen of the windows from the DLS software that we used. In (a), we see the various information introduced by the user or calculated by the software. In (b), we see the ACF. In (c), we see the particle size distribution, in (d) the count rate history (CRH) and in (e), we see the count rate distribution (CRD).*

mounted it on the same rail as the PMT.

3.1.6 The Antivibration table

To mechanically isolate the system from external sources of vibrations we up the entire DLS system on an antivibration table from (Newport Inc.). Since the lab was setup in the basement and the room was well isolated from mechanical and acoustic vibrations, we did not have the need to use the active component of the table's vibration isolation system for our experiments.

3.2 Samples

The samples used in our measurements included polystyrene beads in suspension and metal nanoparticles of a wide range of sizes. More information about metal nanoparticles can be found in [22]. I will also describe the various containers as well as the nanopore arrays used for our experiments. Experiments were performed at room temperature (between 293 °K and 298 °K). Early experiments were performed using tap water, but we soon moved to deionized and filtered water from *Prof. Sinha's group*. The device is provided by *Barnstead E-pure* and provides a Type I water, which is purified deionized and filtered. The final filter is 0.2 μm. Later in our project, we used high-quality distilled water from the group of *Prof. Yitzhak Tor*. The distilled water is provided from a Milli-Q purification system from Millipore. In addition, the Millipore water is also filtered with a 0.22 μm sterile filter (Milipack 40), also from Millipore. The latter water seem to be more pure, because we measured much less scattering from any additional compounds during our DLS measurements.

3.2.1 PS microbeads (0.92 μm in diameter)

The PS (Polystyrene) particles that we used are provided from *Spherotech Inc.* Their size is 0.92 μm (diameter) with a standard deviation of 0.023 μm (or 2.50 %). The concentration is 5.0 % w/v (weight-volume percentage, describing the mass of the solute in g per 100 mL of the resulting solution). They can be kept at room temperature, but should not be frozen. They are stored in deionized water with 0.02 % Sodium Azide. To use them properly, it is recommended to sonicate them. The concentration mentioned above is the one that we call, for simplicity reasons, the *initial* in the other parts of the text.

As mentioned previously, beads scattering experiments are performed in the Mie scattering regime. Interestingly enough, by watching at the suspension, we can see the the milky aspect of Mie scattering regime (Figure 9).

3.2.2 Gold nanoparticles (20, 50 and 100 nm in diameter)

The gold nanoparticles (*NP*) we used during our project is a gold colloidal solution. We have used 20, 50 and 100 nm diameter particles. They are provided from *British Biocell International (BBI)*. They have to be kept at a temperature equal or lower than 4 °C, and are reliable only for several months.

3.2.3 Gold nanoparticles (6 nm in diameter)

The 6 nm gold nanoparticle solution is provided *Ocean Nano Tech LLC* (Springdale, Arkansas). It should be stored at a temperature between 4 to 24 °C. The initial concentration is 10 mg/ml. The solvent is water. The surface ligand is COOH. For our experiments, we diluted them more than initially using filtered and distilled water. (Figure 9)

Figure 9: *Nanoparticle and bead solutions*

3.2.4 AS 15 gold nanoparticles (5-10 nm in diameter)

The gold nanoparticles, (5 to 10 nm in diameter) so called *AS 15*, were provided by *Alberto Schena*, a student working on his master thesis at the UCSD in the group of *Prof. Yitzhak Tor*. They are coated with a thiolic stabilizer (SH groups) having a hydrophilic tail (the $(OCH_2CH_2)_4OH$ terminus) for the water solubility. In those particles, some ligands are replaced by a new one, the acridinium ligand (the one with the tricyclic terminus) which is fluorescent and able to intercalate DNA. This ligand binds the gold surface with a dithiolic/disulfide functionality arising from lipoic acid. Figure 10 shows a representation of a 5-10 nm AS 15 nanoparticle with its ligands.

3.2.5 The Alumina Nanopores

The alumina nanopores that we used are Anopore Inorganic Membranes (Anodisc), from *Whatman*. They are circular anodized aluminum oxide (AAO) membranes with a diameter of 13 mm and an average membrane thickness of 60 μm. Their porosity is between 25 and 50 %. The AAO membranes used in our experiments had a maximum service temperature of 400 °C, and their refractive index is 1.6. We had two different kinds of nanopore membranes: with pore diameter of 100 nm and 200 nm. [23, 24]

3.2.6 The various containers and holders

We primarily used mainly three types of containers. The first type of container was Pyrex Capillary tubes, 90 mm long with an outside diameter of 1.8 mm and an inside diameter of 1.5 mm. The second type of container was microscope coverslips. Their size is 22 x 30 mm and are provided by *Fischer Scientific*. The last type of container was a Pyrex tube with a diameter of 10 mm and a length of 75 mm. Pyrex has a refractive index of 1.474, which is very

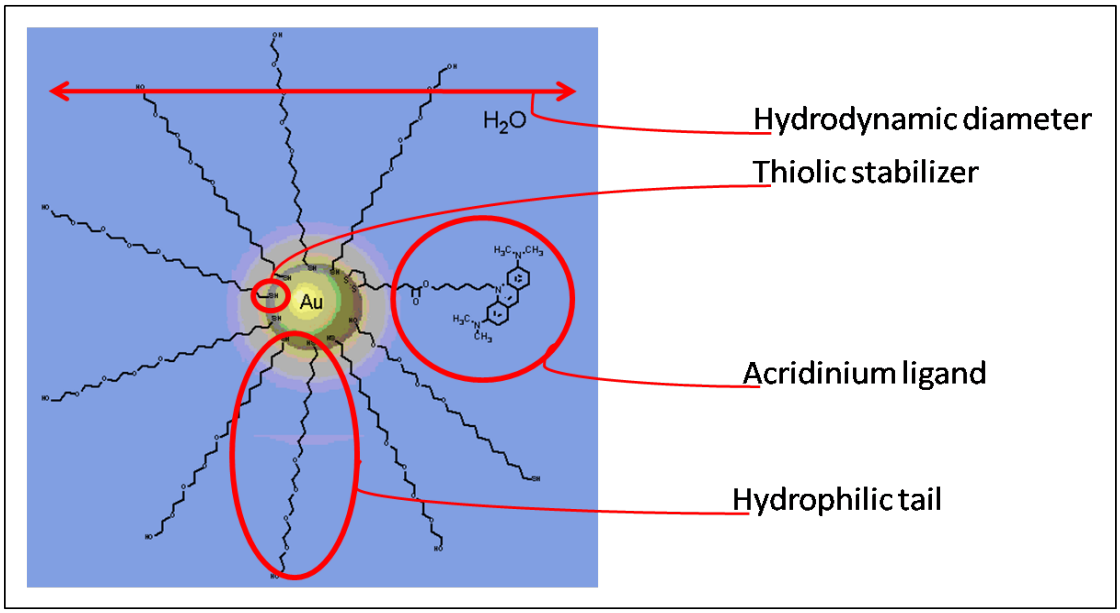

Figure 10: *A representation of a 5-10 nm AS 15 nanoparticle, we see the Thiolic stabilizer (SH groups), the hydrophilic tail ($(OCH_2CH_2)_4OH$ terminus) and the acridinium ligand (tricyclic terminus) and the their hydrodynamic diameter*

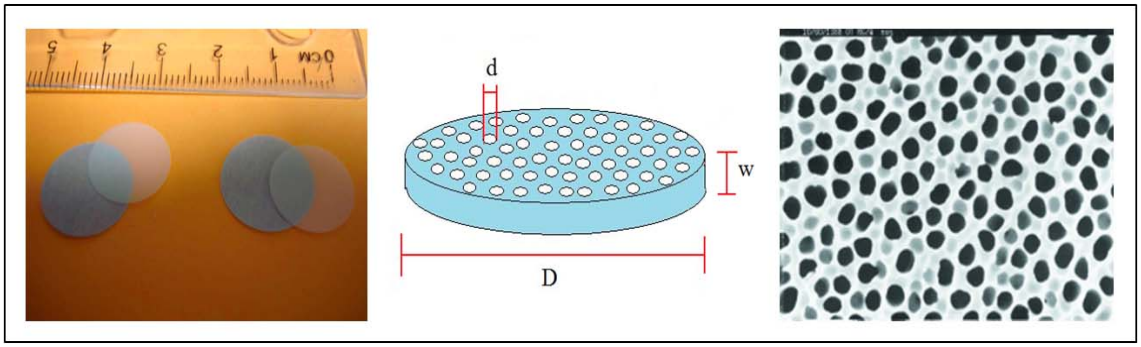

Figure 11: *The alumin nanopore array (membranes). The pores are perpendicular to the plan of the membrane. On the left a real size picture, in the middle a scheme, and on the right a picture from the company at a small scale showing their surface*

close to Decalin.

Figure 12 shows the various containers (Large capillary, Capillary, Coverslips, Pyrex tube with nanoparticle solution and nanopore memnbrane).

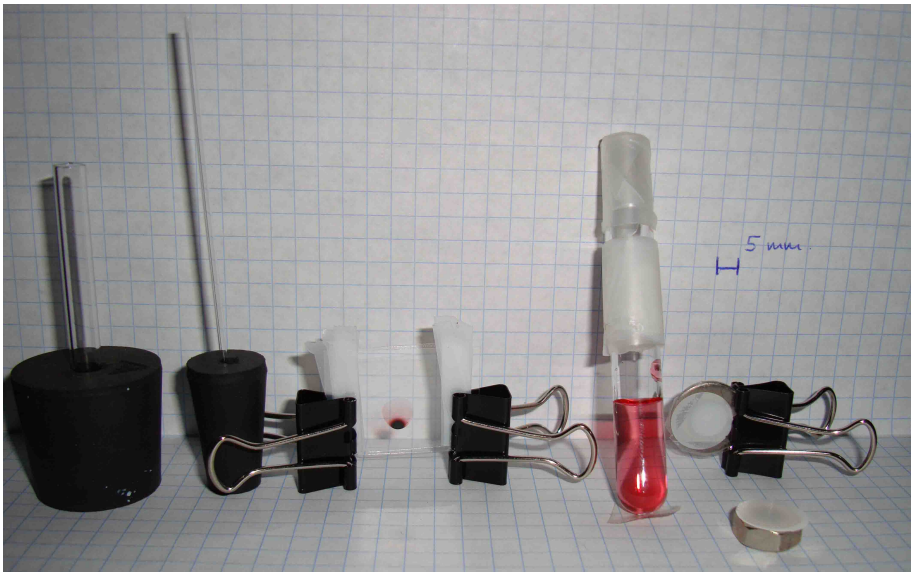

Figure 12: *Our various holders, from left to right, Large capillary, Capillary, Coverslips, Pyrex tube with nanoparticle solution and nanopore memnbrane*

4 Results

We will divide experimental projects described in this thesis in four main parts, the first one being involved in the setup of the DLS instrumentation and in the particle sizing of simple sample. The second one involves experiments aimed at studying the Diffusion coefficient (and particle sizing) of micro- and nano- particles. The third part involves the multi-speckle DLS experiments performed with CCD camera. The fourth part of our work describes analysis of x-ray photon correlation spectroscopy data.

4.1 First steps

4.1.1 Test of the DLS setup with standard milk

In order to test our setup, preliminary test measurements were performed with standard milk. Event though we do not know the exact composition of milk, it is still interesting to test a setup with a simple and very commonplace colloidal solution before proceeding towards more sophisticated samples. Nevertheless, the order of magnitude for sizing results appears to be well within the expected range and the angular dependence is consistent with our expectations (as shown in Figure 14), showing that the measured signal comes really from the sample. The alignment was at this step of the project very rough (implying a small ACF decay), but the results are still quite (qualitatively) reasonable (as shown in Figure 13) The expected the angular dependence to be proportional to

$$\frac{1}{\sin^2\left(\frac{\alpha}{2}\right)} \tag{35}$$

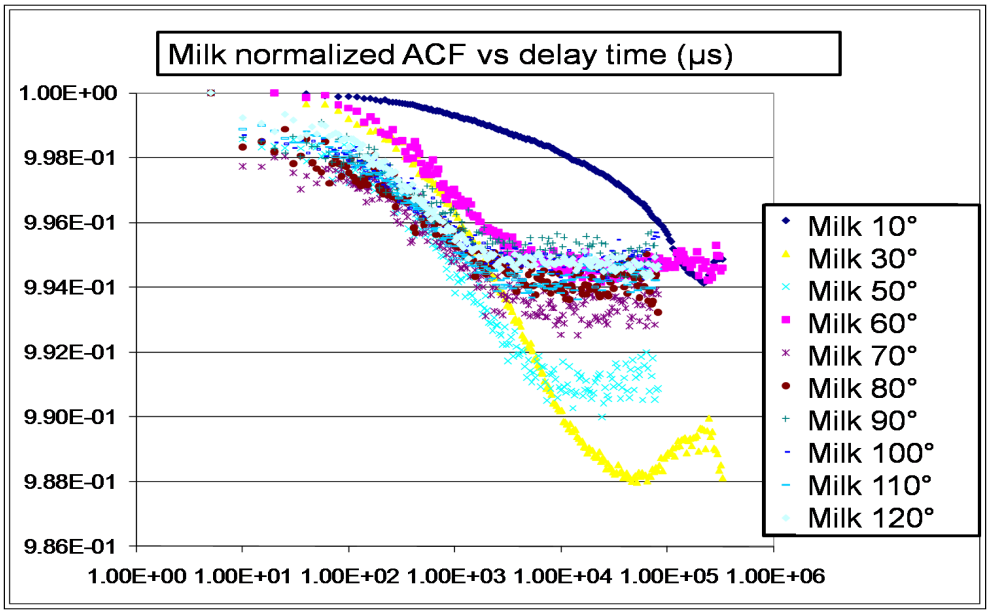

Figure 13: *Normalized ACF obtained with standard milk. The decay is small but the angular dependence is obvious.*

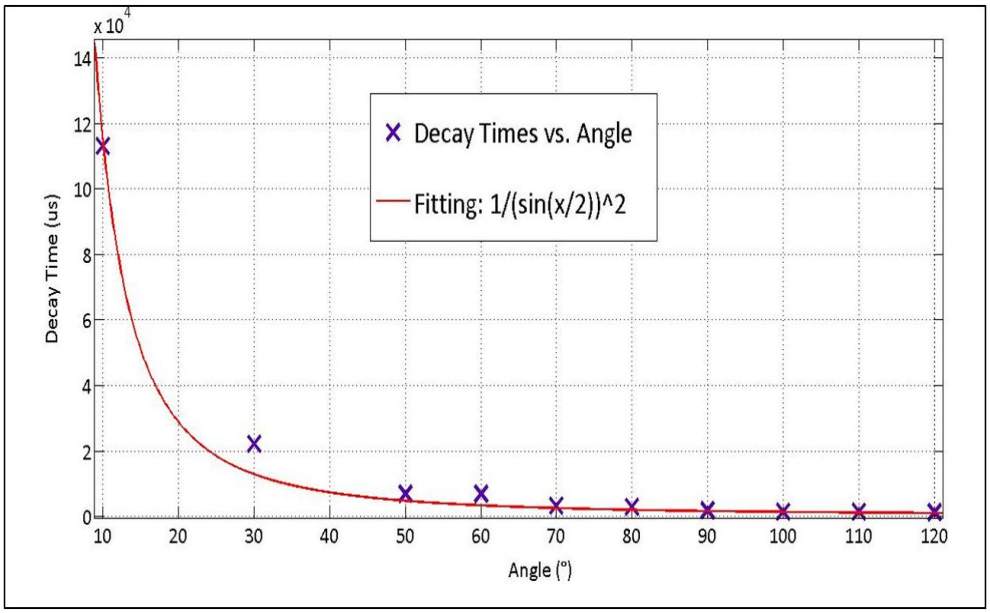

Figure 14: *Angular dependence of the time decay for standard milk. There is obviously an angular dependence.*

4.1.2 Alignment

The alignment of the DLS setup is a quite long procedure. The main difficulty of the alignment resides in the fact that a high precision requires to place the sample exactly at the goniometer center rotation. Furthermore, the lens should also focus on this point, and the four elements (laser, lens, center of the sample holder and detector) have to be on a line.

The First step is to align the laser with the goniometer and the detector. At the beginning of the project, we had only a simple laser mount, which didn't allow other freedom of motion than the rotation around the rod and the height of the laser. Later, we ordered a much more sophisticated laser mount allowing more degrees of freedom for a more precise orientation of the laser. In turn, we mounted the rod with the laser mount and the laser on a movable stage. As a consequence, we also had a more precise control of the height and a short range translational freedom.

The laser being aligned with the goniometer and the detector, the lens should be added and a readjustment of the complete system is necessary. For the reasons described in section 3.1, the company provided with the DLS setup a matching index vat as well as a matching index liquid (Decalin). The introduction of the vat requires some additional steps in the alignment. The next step in the alignment process is the detector optics adjustment.

The last step of the alignment, which turned out to be the most time consuming was to find the rotation center of the goniometer (it has to fit with the rest of the setup). The company furnished us a precisely machined needle that can be put in the exact center of the manifold. Using the diffraction of the laser beam on the needle tip and changing the angle, by an iterative process, we can theoretically reach precisely the rotation center. It is also very difficult to move accurately the sample holder plateau, which renders the procedure even more complicated. This alignment is then done by iterations of the different steps.

A full alignment of the process can take around 2 or 3 days (if the system is completely misaligned). Several times, we did experiments with a shorter alignment procedure which consists of an adjustment of the detector optics in order to have a high intensity passing though. The purpose is to be sure that our detector receive enough scattered light. It is a reasonable process if we don't need very precise measurements.

In the following part of the project, since we are more interested in the understanding of the phenomena, than to get precise results, we alternatively used the PS beads and the nanoparticle suspensions.

The pinhole of the detector optics has six diameters available (0.1, 0.2, 0.4, 1, 2 and 3 mm). The intensity of the incident light depends on the pinhole size. The larger the pinhole

diameter, the higher the intensity of the incident light. The decay of the ACF is smoother with large pinholes than with small ones. In the Figure 15, we show normalized ACFs and related intensity histories obtained at 90° with PS microbeads for the six available pinholes. The results follow our expectations. An appropriate choice is to have a pinhole diameter comparable with the speckle size. If the measured intensity is very low (measurements of small nanoparticle dynamics is an example), it is appropriate to use a large pinhole, which reduces the Siegert factor of the ACF but gives an enough intense signal to be measured.

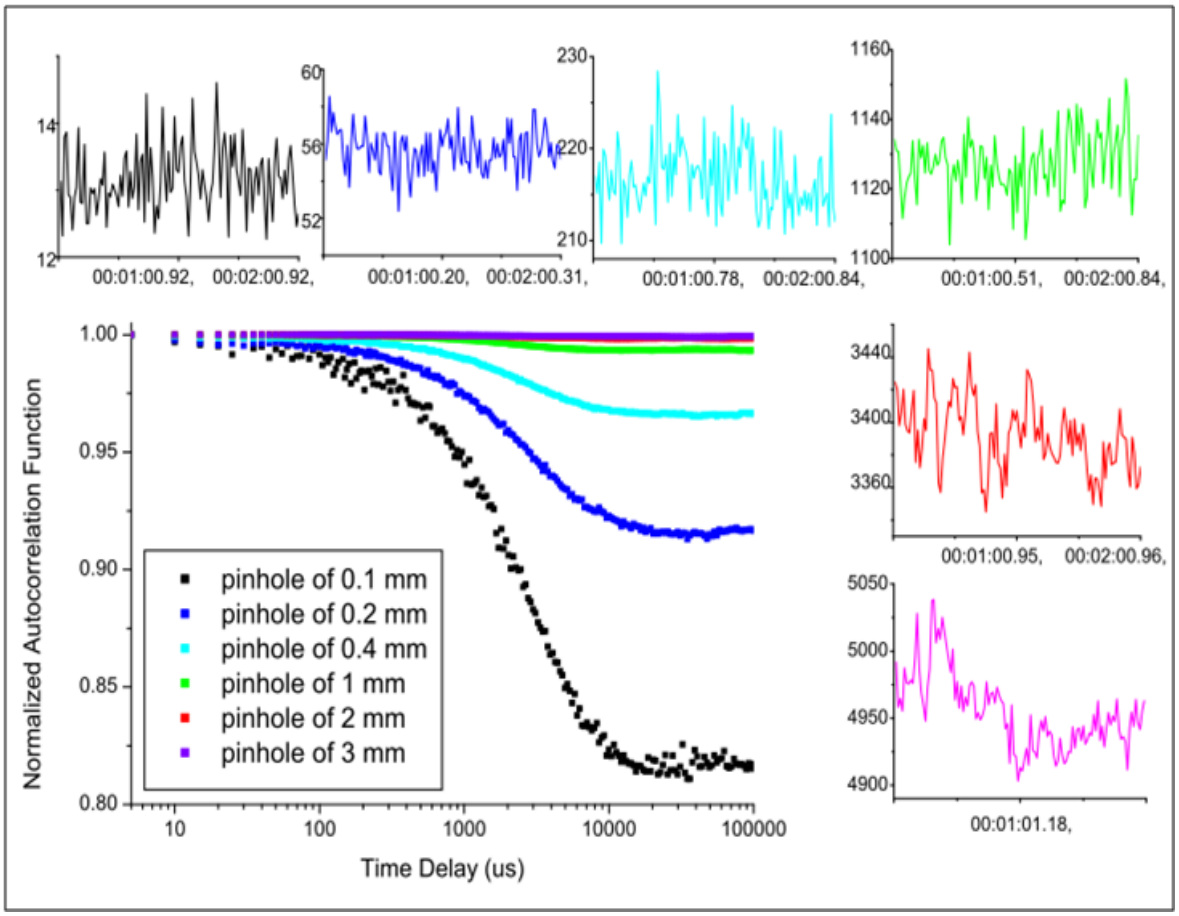

Figure 15: *Intensity measurements and normalized ACF token with microbeads for various detector optics pinhole sizes.*

4.2 Data analysis

Before describing the results, I will briefly write about the procedure used to obtain the particle size and the diffusion coefficient.

In the case of the PMT, the autocorrelation function was done by the correlator, as mentioned previously. The software gives the data in standard ASCII format (.dat). It was thus easy to import them on *MATLAB*. For the ACF fittings, we used the toolbox *Curve fitting*. This toolbox allows to fit the ACF with a summation of two exponentials. It is also possible to introduce exclusion rules. Depending on the shape of the ACF, especially on the flat part before and after the decay, we excluded a part of the delay times in order to get a more accurate fitting. As a fitting function we used.

$$f(x) = a\exp(bx) + c\exp(dx) \tag{36}$$

This fitting provides us the decay time. Then, for the diffusion coefficient calculation or particle sizing, we can use equations (4), (21), (20) and (22).

In the case of the CCD camera, since the software provided us an image with the measured intensity for each pixel, we still had to correlate it with *MATLAB*. The two possible ways are either to correlate it using a standard correlation done with *MATLAB*, or to find out the decay time, by calculating eq. (27) as described in section 2.5. Using this process, shown in Figure 16, we obtained the result shown in section 4.7.

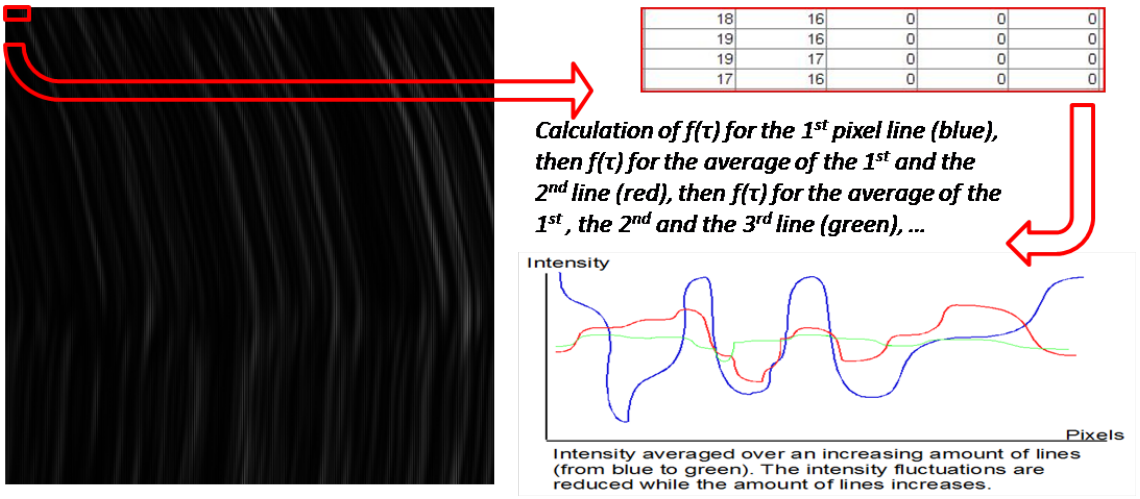

Figure 16: *Schematic illustration of a non usual method allowing time-varying (non-equilibrium) dynamics study. We see the CCD image (left) imported as a matrix (up right) in MATLAB (where each pixel intensity is a number) yielding fluctuations (down right) which decrease with the amount of averaged lines.*

4.3 Polystyrene (PS) microbeads

With the PS beads (0.92 μm in diameter) we could improve a lot the accuracy of the results. We do not display here all results obtained, but only the ones corresponding to the main steps of improvement. Before to reach accurate results, we tried several different containers. The alignment was greatly improved during those experiments.

The first sample container was the capillary. The main problem with this container is the light diffracted from the edge of the capillary. This diffracted light formed a very bright line across the lab, and therefore passing also through the detector optics. The accuracy of the results obtained with this configuration is quite low. The reason is the presence of a local oscillator (bright line), which requires a heterodyne method, but we worked with the assumption of a homodyne experiment.

In order to avoid this effect, we tried the same experiment but using two coverslips. The results are with this configuration much more accurate but the disadvantage is that the solution solvent evaporates very quickly and after a short time any fluctuation is lost. Another disadvantage is that the coverslips have no cylindrical symmetry, which makes the angular dependence study more difficult.

In order to avoid the inconvenience of the bright line related above, to use of tubes, or very large capillaries (cylindrical symmetry) is possible. A requirement is that the capillary diameter is much larger than the width of the focused laser beam. In fact, by using tubes, it is easy to focus the light at their center. The laser passes through the roughly perpendicular tube glass wall and is scattered by the particles in suspension. The cylindrical sample symmetry offers the possibility of angular dependence studies.

The introduction of the index matching vat prevents big refractive index differences in the path of the light. The vat can be filled with pure water or with decalin (matching refractive index). There is still some difference in the refractive index of water (of the suspension) and of decalin, or pyrex (very close refractive index) but much lower than between air and pyrex.

We show in Figure 18 an interesting result which shows the reproducibility of our measurements as well as the similitude between the diameters obtained with the fittings done from *Brookhaven*'s software and our fitting on *MATLAB*. We did two experiments, on two different days, with two different samples (both with our PS beads). We assume that the setup was aligned, the only possible source of misalignment is the sample. In the Figure 17 we see the normalized ACF from the first experiment. The ones from the second experiment are similar. In both cases the decay is in the order of several %, as shown in Figure 17 for the first experiment. The Figure 18 show the particle sizes obtained for both experiments. We believe that the smaller values than expected at small angles are due to multiple scattering and the larger

ones at big angles are due to the presence of additional larger compounds in our solution. The polydispersity is here always below 0.4 and mainly below 0.3.

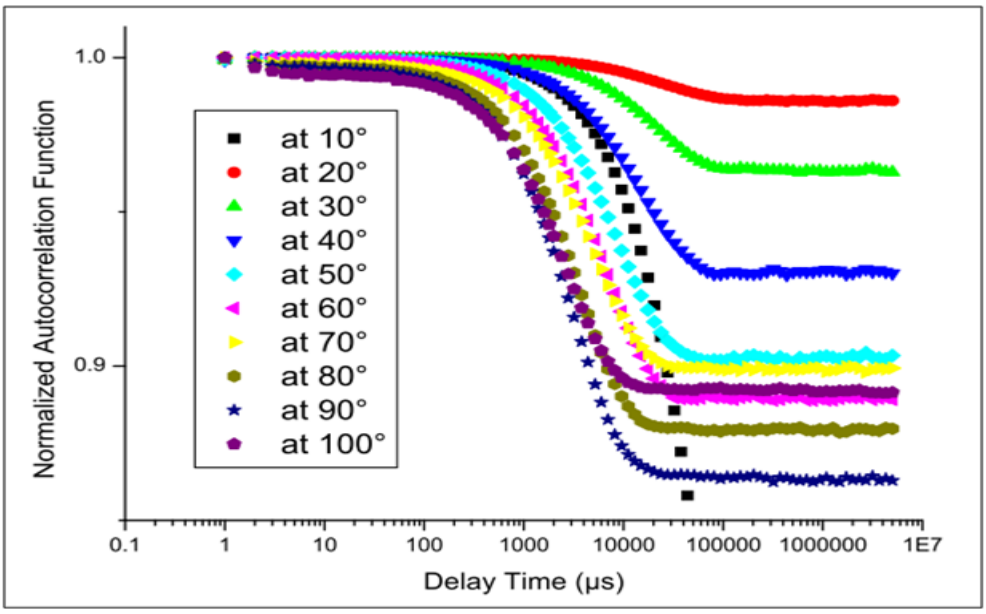

Figure 17: *Normalized ACF for different angles for PS beads. The angular dependence is the expected one, and the ACF decay is in the order of several % (except at 10°, in the order of 80 %, not completely shown)*

Figure 19 shows a plot with concentration and angular dependence. The results are quite good, they show the reproducibility and the expected angular dependence. The concentration plays a minor rule, as expected in this concentration range. the small particle sizes obtained for small angles are very probably due to multiple scattering, and other issues, as discussed in section 5.5. As in the previous results, the smaller particle sizes obtained for small angles are very presumably due to multiple scattering, and at bigger angles the larger particle sizes due to the presence of additional larger compounds. The polydispersity is here always below 0.4 and mainly below 0.3.

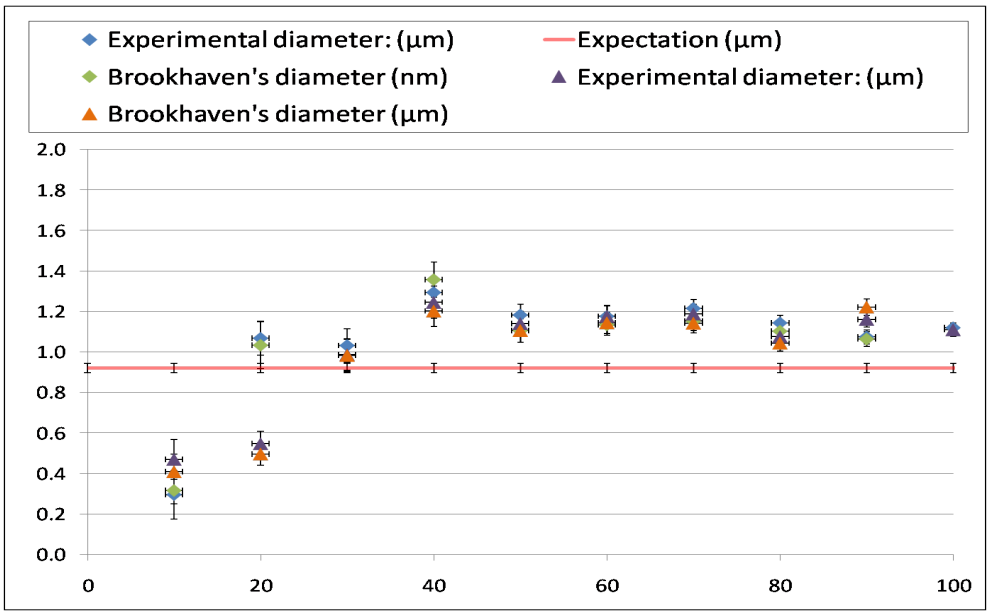

Figure 18: *Particle sizes obtained for two experiments done in the same conditions but different samples and on different days, at various angles. This plot also shows that our particle size calculation (through the fitting done on MATLAB) is consistent with the one from Brookhaven. The results are close to the expectations, except for small angles.*

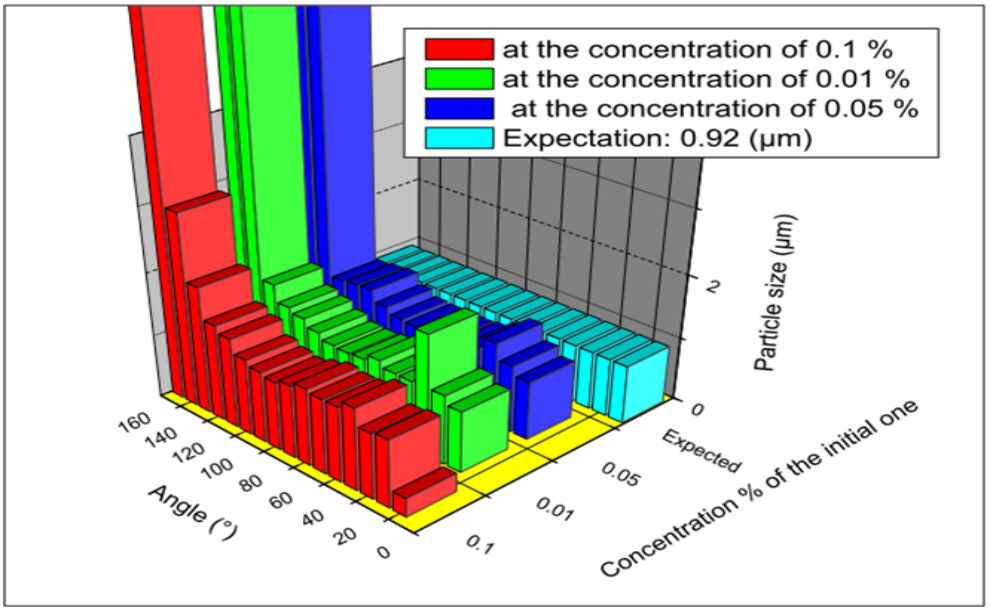

Figure 19: *particle sizes obtained for various angles and concentrations. We see the reproducibility of our measurements for various concentrations as well as the smaller particle sizes obtained for small angles. The concentration is given in % of the initial one, which is 5 % w/v*

4.4 Gold nanoparticles

Turning now to nanoscale particles, we first describe the results obtained for 100, 50 and 20 nm (in diameter) gold nanoparticle. Since the size is ca. 10 times smaller and more than the microbeads, the intensity of the scattered light is much smaller, which induces new challenges for their study.

4.4.1 100 nm (diameter) nanoparticles

In the first result that we show, the ACFs undergo a decay of ca. 2 % (except at 5°) (Figure 20). The decay times follow the expected angular dependence (Figure 21) and the particle sizes are in the good range (Figure 21), but still below the expectations (could be due to multiple scattering).

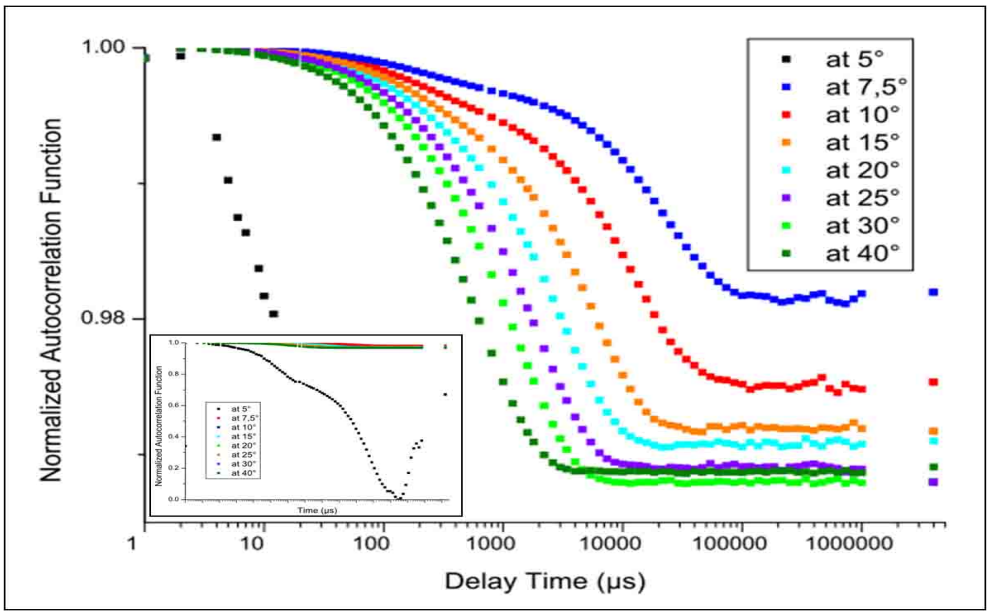

Figure 20: *Normalized ACF for gold nanoparticles (100 nm in diameter) at various angles. At small angles, there is a smooth second decay (related to faster dynamics).*

The following result (Figure 22 and 23) is interesting, because it clearly shows two decays in the ACF at small angles. In Figure 23, at 5°, 7.5°, 10° and 15°, the two values represent two different fittings. The larger particle sizes are obtained by fitting only the decay at larger delay times, corresponding presumably to our 100 nm gold particles. If this is the case, we can see the clear difference between an additional signal and our nanoparticles. This result is surprising, the presence of a faster dynamics could be due or to smaller scatterers or more probably to a local oscillator or other experimental issue.

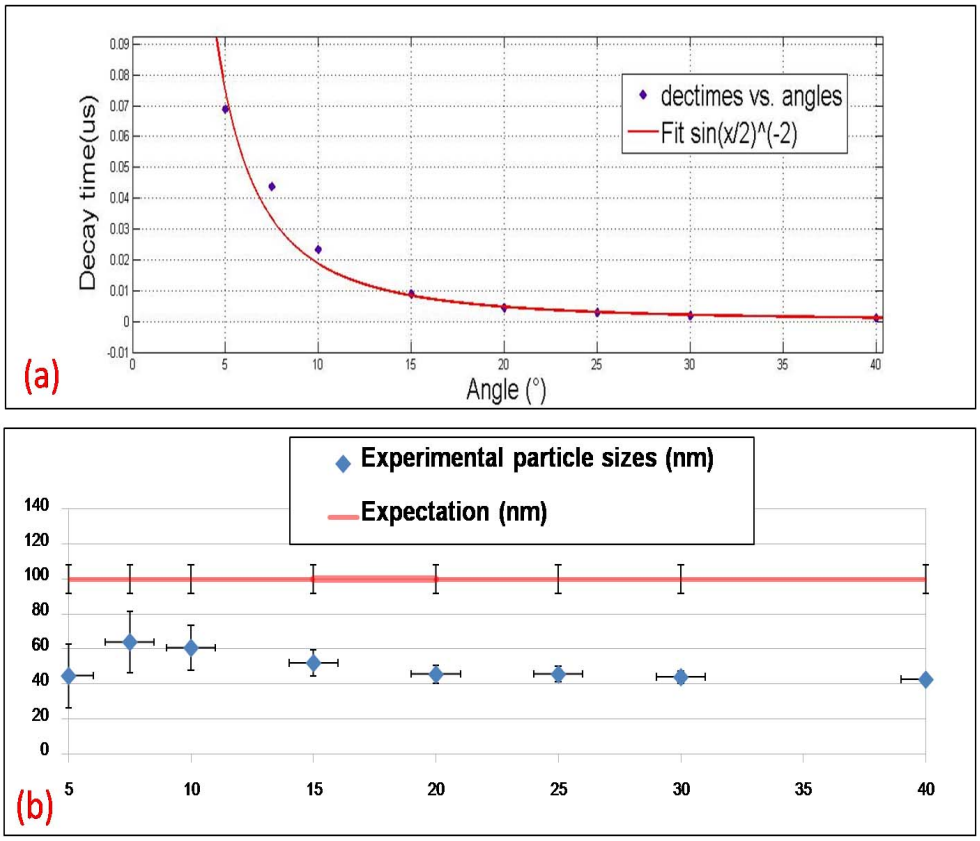

Figure 21: *(a) Angular dependence (5° to 40°) of decay times for gold nanoparticles (100 nm in diameter). (b) Particle sizes obtained (lower than the expectations). It seems that we still have some angular dependence in the sizes.*

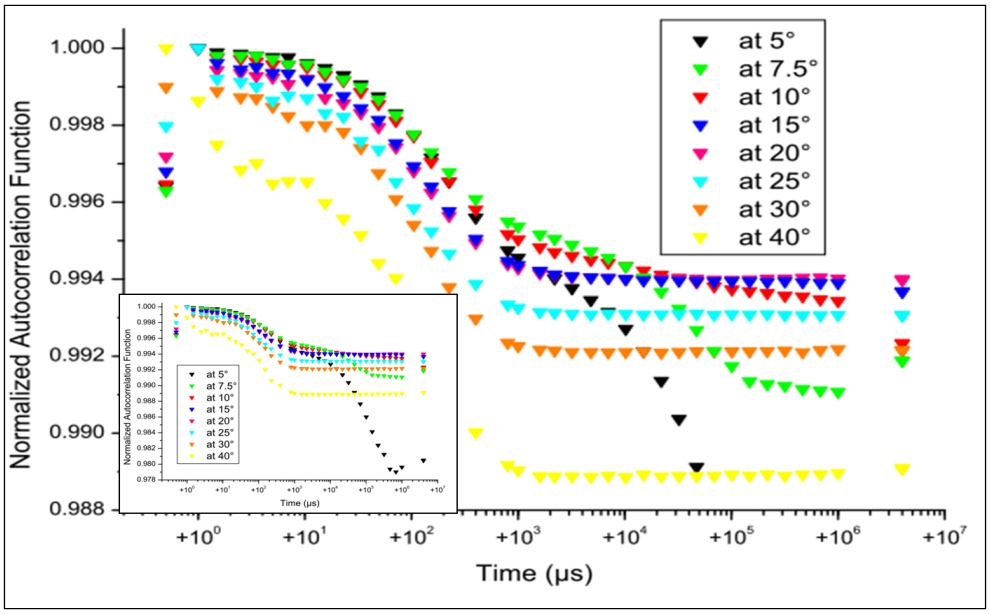

Figure 22: *Normalized ACF for gold nanoparticles (100 nm in diameter) at various angles. At small angles, we see two decays, one at shorter delay times and the other one at larger delay times. The ACF undergo a smooth decay (close to 1 %).*

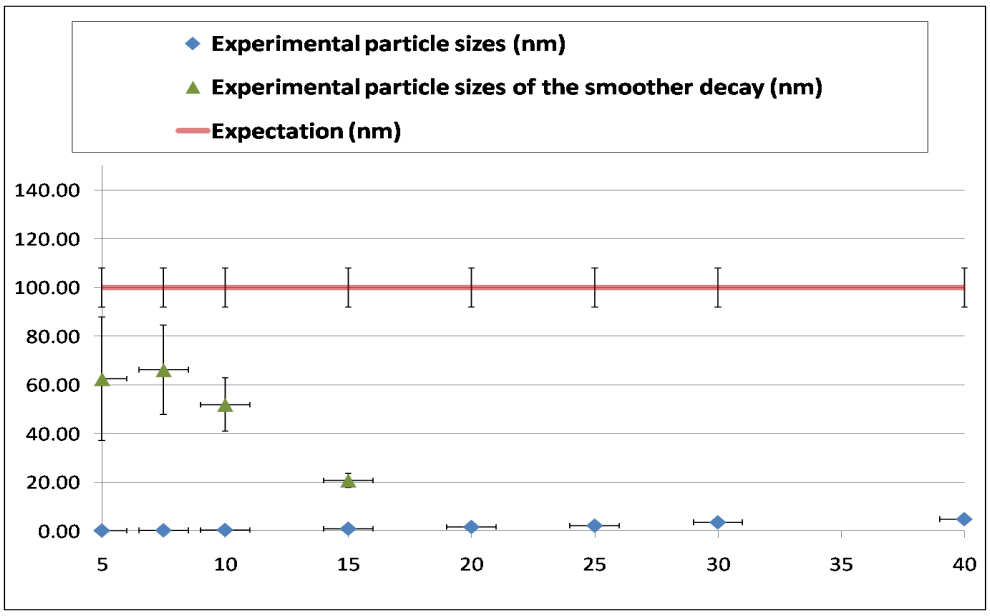

Figure 23: *Measured particle sizes for gold nanoparticles (100 nm in diameter). We see two different particle sizes, corresponding to the fitting either from the first decay or from the second one.*

4.4.2 50 nm (diameter) nanoparticles

After a precise alignment of the DLS setup, we could obtain enough signal from the 50 nm nanoparticles. We see in Figure 24 that the decay of the correlation function is accurate and in the order of 5 %. Figure 25 shows that the particle sizes obtained from the ACF are in the good range, except for small angles. The reason is probably the presence of a local oscillator or additional compounds. At larger angles, the particle sizes are still above the expectation, probably also due to other scatterers larger than 50 nm. The polydispersity this experiment is between 0.2 and 0.34.

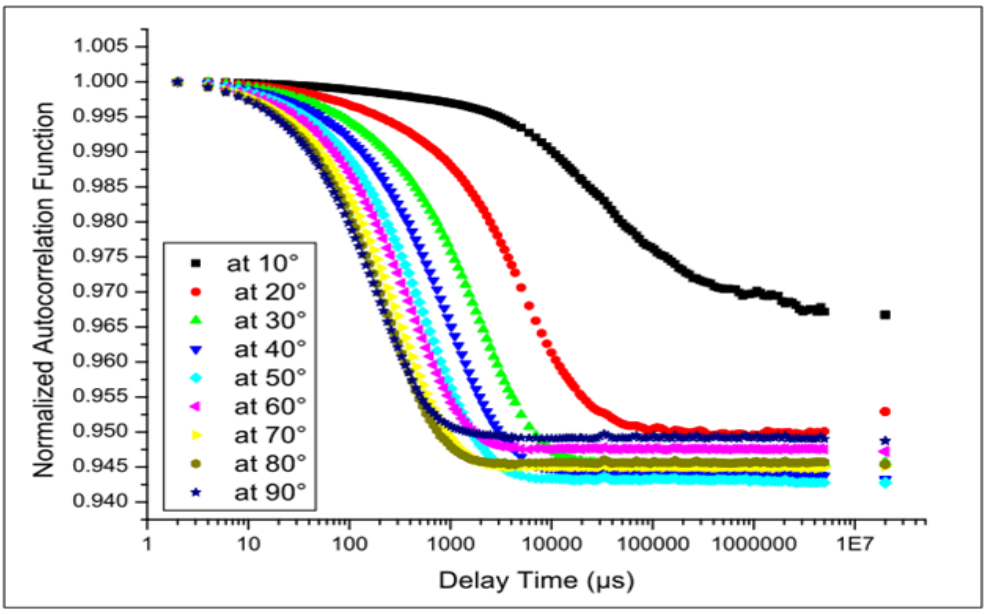

Figure 24: *Normalized ACF for gold nanoparticles (50 nm in diameter) at various angles obtained after a precise alignment of the DLS setup.*

Instead of showing the decay times vs the angle, as shown previously, we can also plot the inverse of the decay time ($1/\tau$) vs q^2 which has the advantage to be linear and (see equations 21 and 20) . Figure 26 shows this linear dependence obtained for the same experiment. We see the expected q dependence.

In the following graph, we see results which were obtained in cleaner condition than the previous. In fact, after the various experiments done with the 6 nm nanoparticles, we concluded that the main error in our results were due to compounds present in the suspension. Therefore, we repeated the 50 nm nanoparticle sizing after a meticulous cleaning with sonication.

For small angles ($<$ than 25°), we used a box to diminish the possible air flow and various external influences. We introduced a tube in front of the detector optics for the same reasons

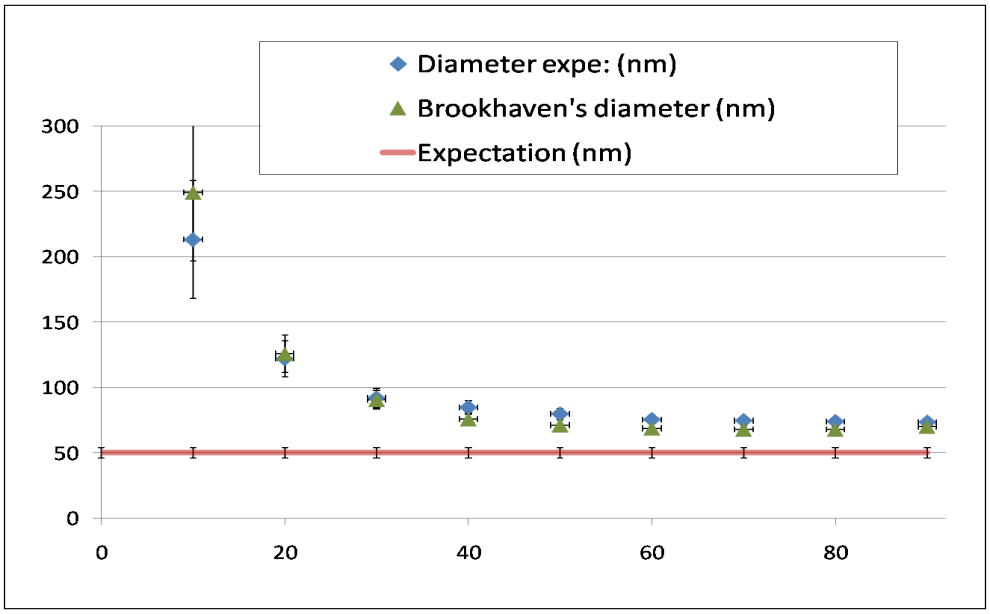

Figure 25: *Measured particle sizes for gold nanoparticles (50 nm in diameter) vs angle. The particle sizes are in the expected range for at larger angles than 30°. We suspect the presence of additional compounds larger than 50 nm, and maybe of a local oscillator at small angles.*

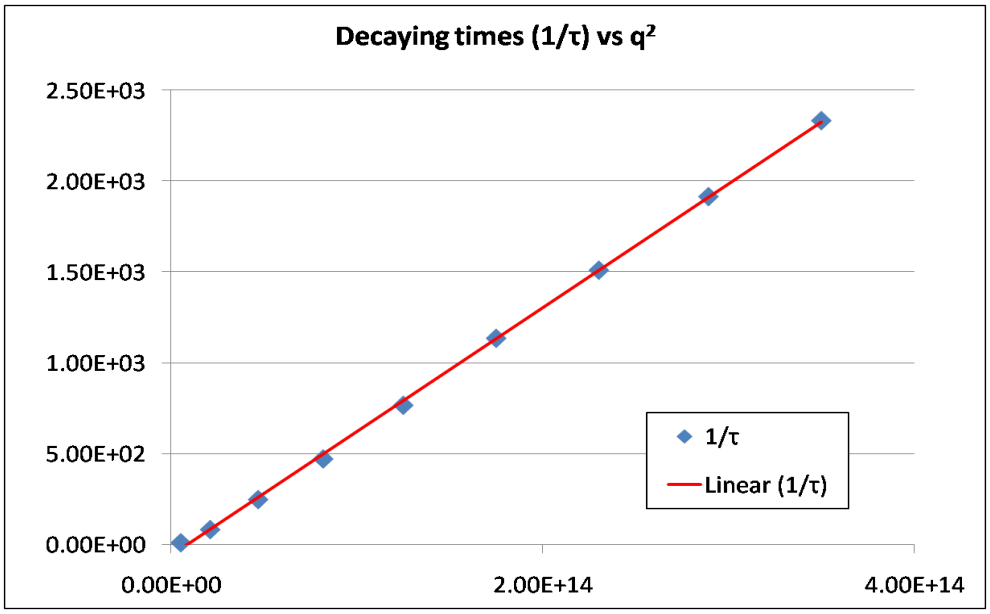

Figure 26: *q dependence of the inverse of the decay time for gold nanoparticles (50 nm in diameter), after a good alignment of the DLS setup. We see the expected linearity.*

(see Figure 34). The measurements were token over a total duration of 5 min for each angle, and repeated a second time in order to increase the average time to 10 minutes gives better statistics. Figures 27 and 28 show the results. Figure 27 shows the normalized ACF and Figure

28 shows the calculated particle sizes, at several angles. The polydispersity is in this experiment is between 0.075 and 0365, the higher values obtained at small angles (which corresponds with the particle size accuracy).

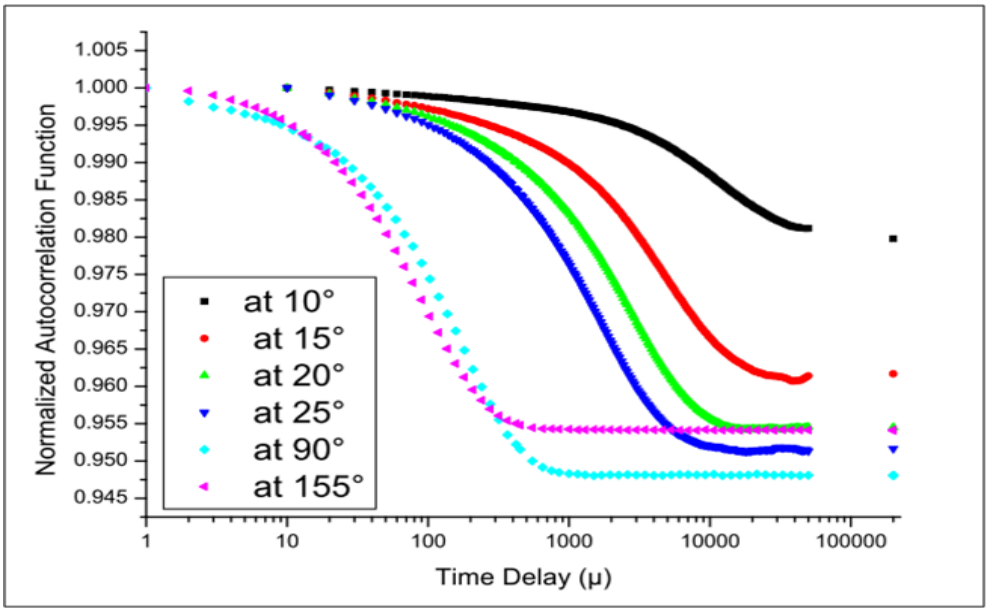

Figure 27: *Normalized ACF for gold nanoparticles (50 nm in diameter) at various angles obtained after a precise alignment of the DLS setup, a meticulous cleaning of the sample and an isolation from external influences.*

The Figure 29 shows, like for the previous result, the inverse of the decay times ($1/\ \tau$) vs q^2 . We see again clearly the expected linear dependence.

As a consequence, we see that the experimental approach described above (good alignment, meticulous sample preparation and isolation from external influences) is a requirement for accurate results with nanoparticles. The remaining imprecision (measured particle size slightly above the expectations (see Figure 28)) will be explained in the following section.

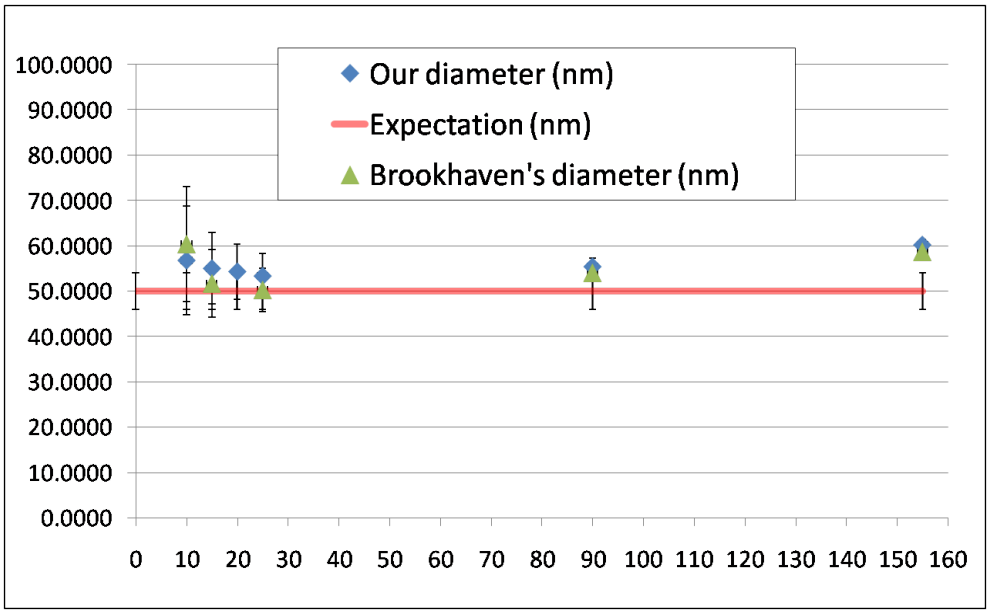

Figure 28: *Measured particle sizes for gold nanoparticles (50 nm in diameter). After a precise alignment of the DLS setup, a meticulous cleaning of the sample and an isolation from external influences we see a clear improve in the measured particle sizes.*

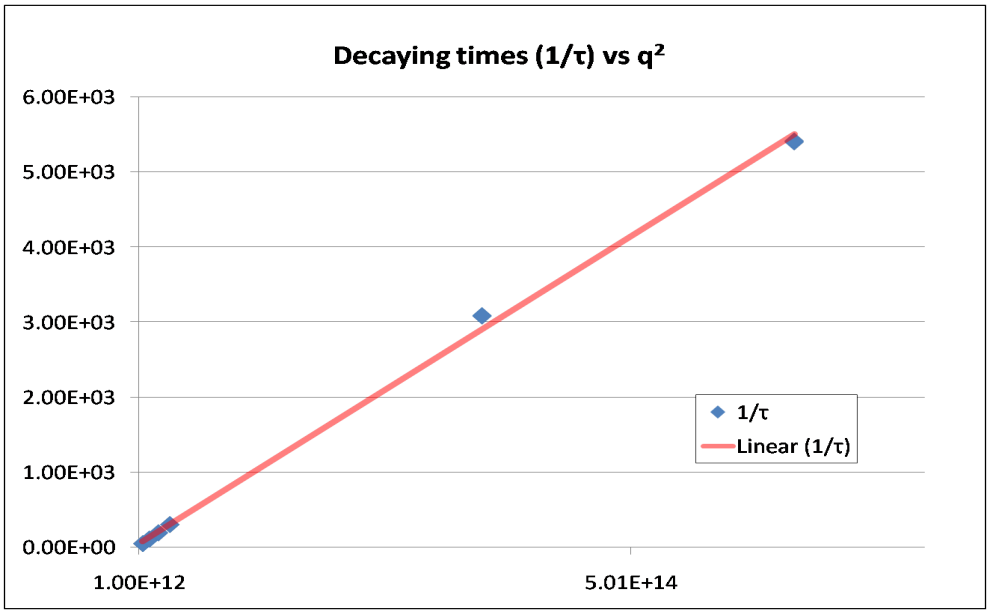

Figure 29: *q dependence of the inverse of the decay time for gold nanoparticles (50 nm in diameter) with isolation from external influences, good alignment and meticulous sample preparation. We see the expected linearity.*

4.4.3 20 nm (diameter) nanoparticles

The study of 20 nm nanoparticles induces some experiment challenges. An important one is to have good alignment in order to measure a sufficient intensity and an other one major one is to have no additional compounds, larger than the particles in the solution, which basically requires a good sample preparation and the use of very pure water.

In those conditions, we could obtain the normalized ACF shown in Figure 30. For all angles, we used the tube in front of the detector optics to diminish external contributions (Figure 34). The measurements were token over a total duration of 10 min for each angle.

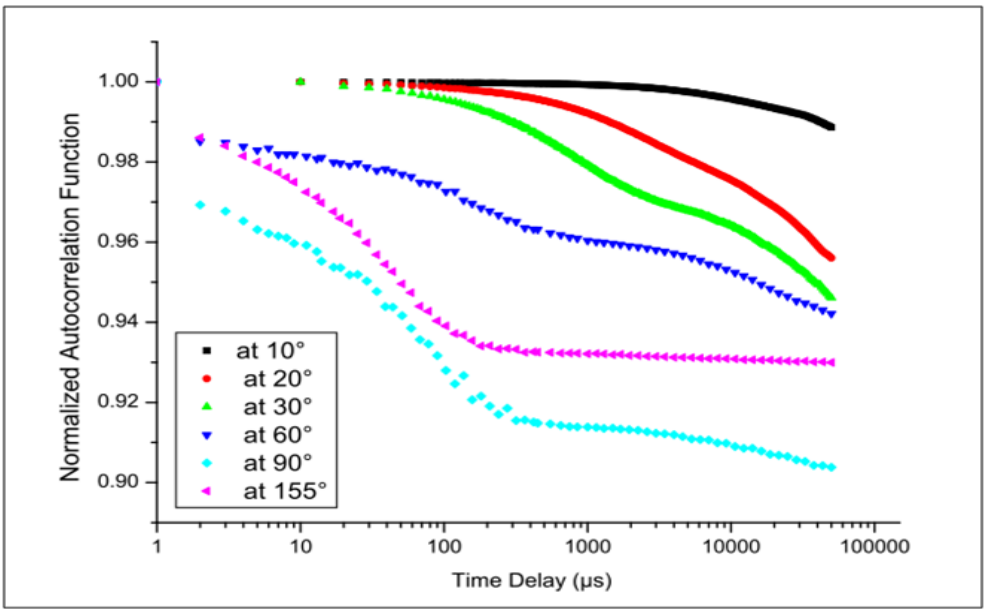

Figure 30: *Normalized ACF for gold nanoparticles (20 nm in diameter) at various angles.*

For small angles the results are not representative of our particle sizes. In fact, for larger angles, we see two decays. we can assume that one comes from our particles, and the other one from some unwanted additional scatters in the solution. Since for small angles the intensity is very high, we can assume that the unwanted scatters (much larger than the nanoparticles) give a strong contribution in the ACF. Therefore, at small angles, we cannot see the contribution from our particles. This idea is confirmed by the great amount of high intensity peaks that we have at small and large angles (see Figure 31). Close to 90°, the amount of high intensity peaks is reduced. This is not a surprise, because it is expected (among others, for geometric reasons) that the contribution of various imprecision sources, such as multiple scattering or additional compounds, play the smallest role at 90°.

In the Figure 31, we see the history of the intensity. The large amount of high intensity peaks confirm our assumption, which is that we have additional compounds in our solution.

If we take into account only the "continuous" low intensity, we mainly reach the expected particle size. But, since we also take into account the high intensity peaks, our decay times are shifted to slower dynamics, which implies much larger particle size estimation.

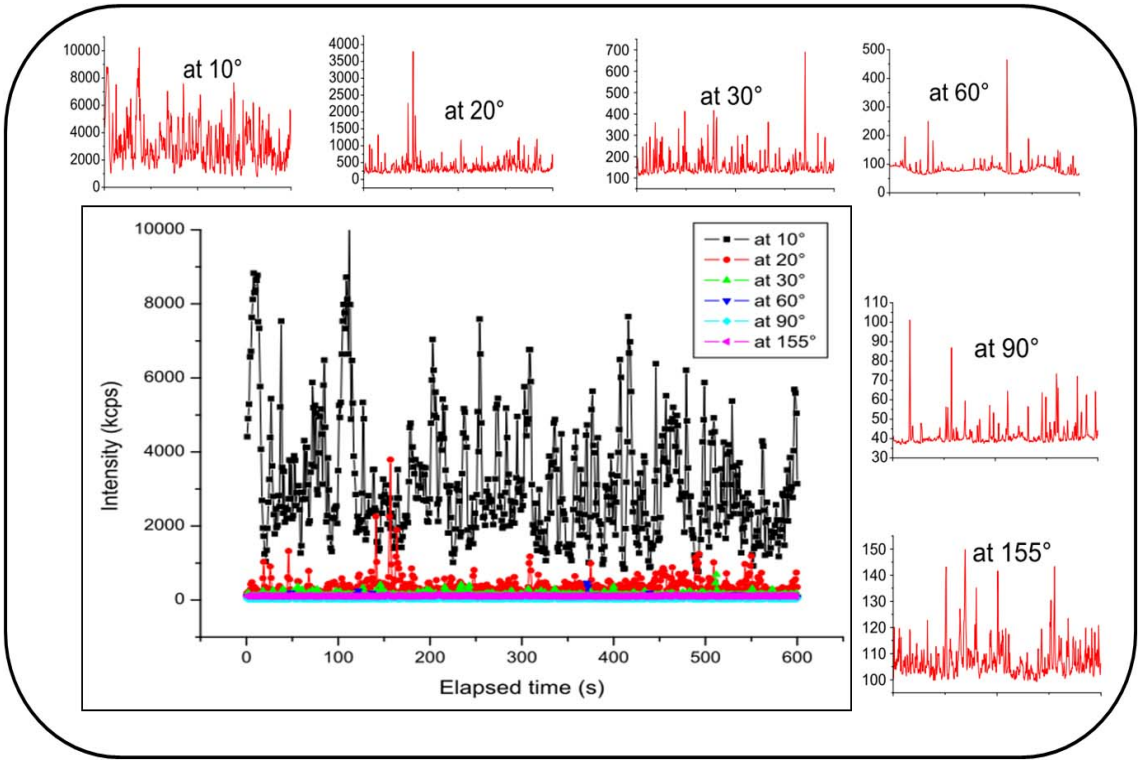

Figure 31: *Measured intensity for gold nanoparticles (20 nm in diameter) at various angles.*

As mentioned above, in order to confirm our assumption, we took several short runs of 30 seconds, at 90° and 155°, selecting the ones which have only few high intensity and small peaks. Then, making an average of the selected runs, we get better statistics (longer average time, 2 min and 2 min 30 sec in the Figure 32). With this approach, we can expect that the particle sizes are closer to our expectations. The previous appeared to be an interesting method to improve the results, having additional large compounds in solution.

In the Figure 32, we selected 5 (for 90°) and 4 (for 155°) runs, where we have few additional events (high intensity peaks). Each run took 30 seconds, thus the average is done over 2 min 30 sec (for 90°) and 2 min (for 155°). We see that the results are close to the expectations (Figure 33).

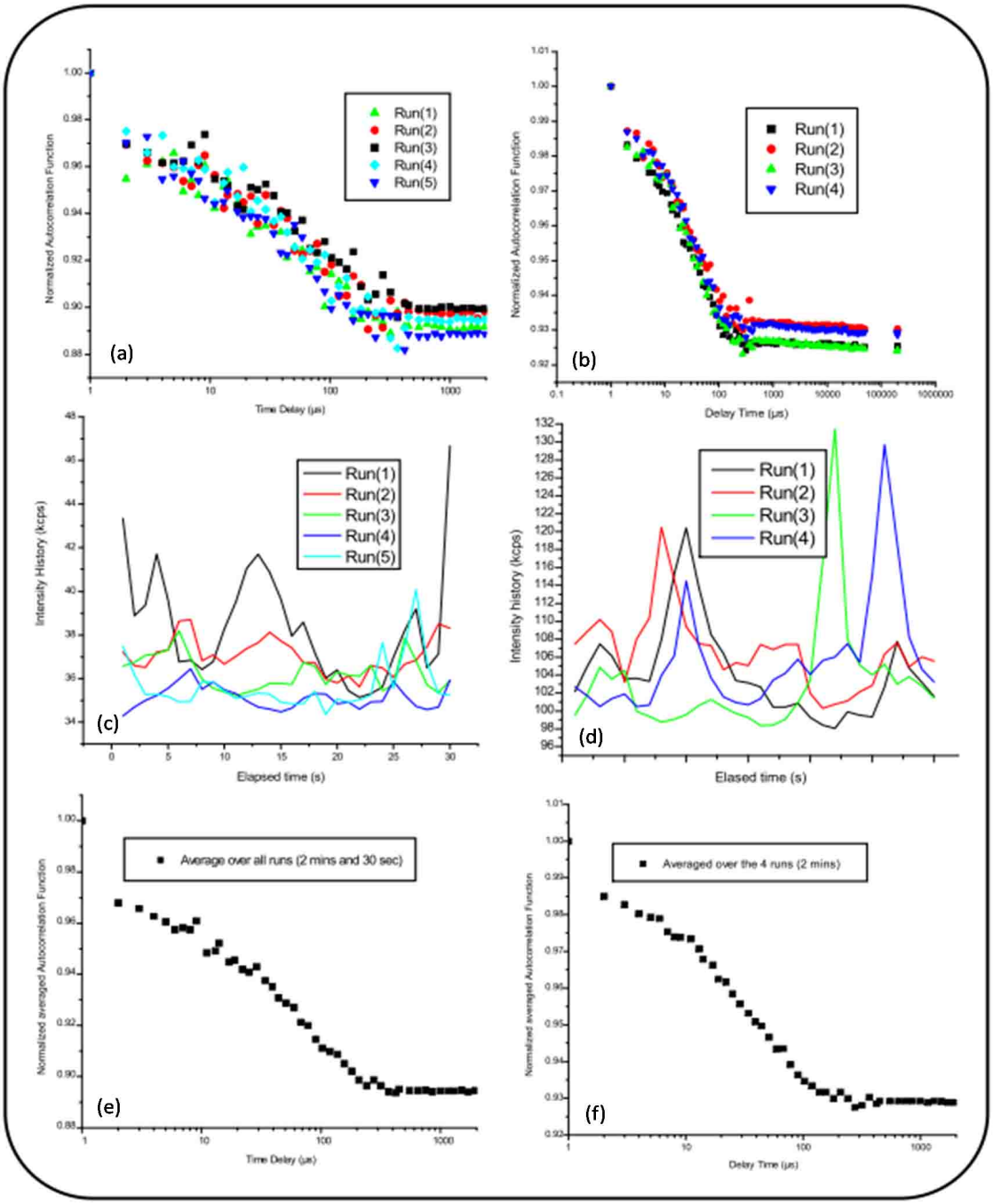

Figure 32: *Normalized ACF and count rate history (CRH) for gold nanoparticles (20 nm in diameter) at 90° and 155°. By selecting 30 sec runs having few additional lower events (high intensity peaks) we can improve the particle size measurements (shown in 33)*

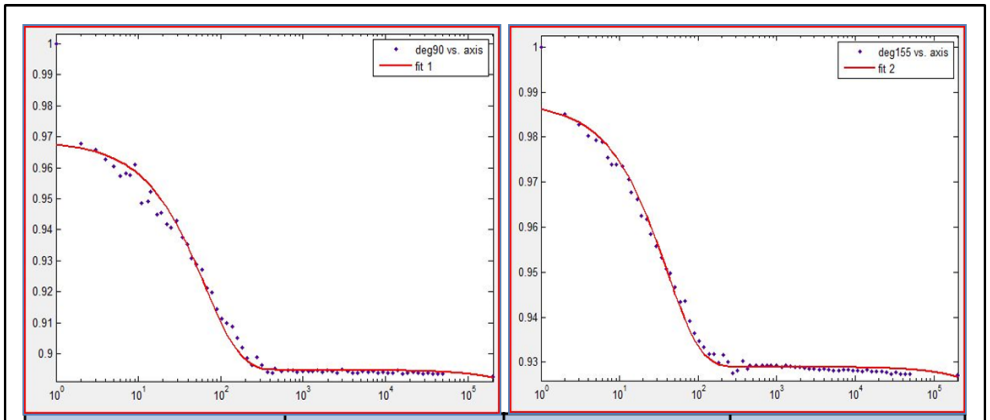

Particle sizing	At 90° (nm)	At 155° (nm)	Expectation (nm)
	21.97	25.76	20.00

Figure 33: *Accurate measured particle sizes for gold nanoparticles (20 nm in diameter), at 90° and 155°, after a selection of runs with few unwanted events, and the fits from MATLAB*

4.4.4 6 nm (diameter) nanoparticles

The difficulty with 6 nm (in diameter) nanoparticles is that the scattered light intensity is much lower than the one from 20, 50 or 100 (in diameter) nm particles. The problem comes mainly from the laser wavelength, which is 633 nm. In order to measure the particle dynamics, we would like to have a laser wavelength roughly of the same order than the scatterer diameter (see eq. 13).

We had no signal coming from the 6 nm gold nanoparticles, but some signal coming very presumable from larger scatterers in suspension. To make sure that we have no dust passing through our laser beam, and that the additional events come really from the solution, we added a box and a tube around the laser beam, as shown in the Figure 34.

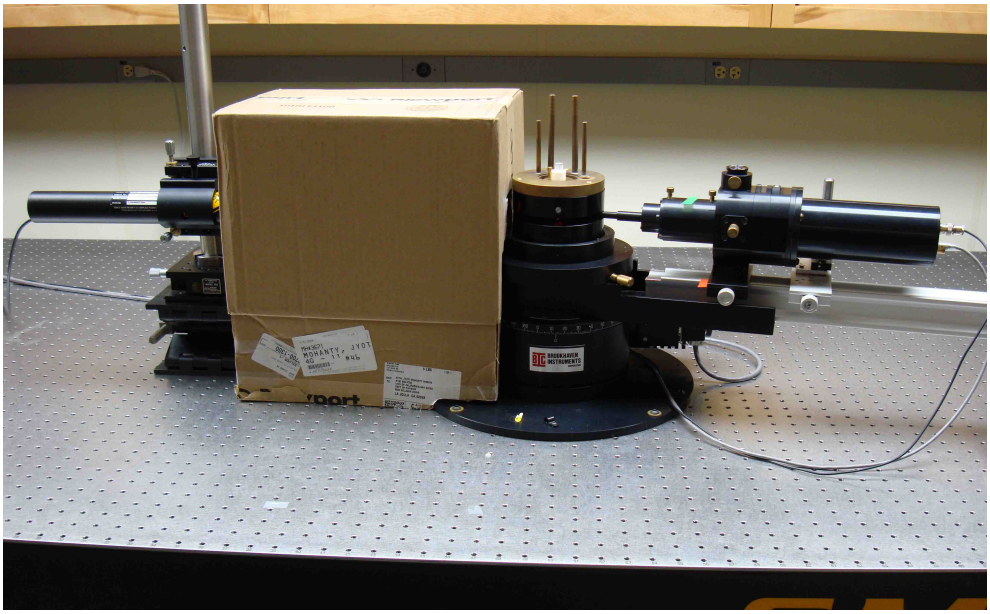

Figure 34: *Our DLS setup with air flow and external light isolation (tube and box).*

Obtaining no other signal than the high intensity peaks, we can assume that the measured signal comes only from larger scatterers in our colloidal suspension or maybe from nanoparticle aggregations.

The sonication, just before measuring, tends to increase even more the high intensity peaks. In fact, some dusts could be stuck on the container wall or precipitated and mixed with our nanoparticles during the sonication. For our experiments the sonication should be used only to clean the containers and various other tools.

4.4.5 5-10 nm (diameter) nanoparticles

We repeated the experiment with the AS 15 nanoparticles, having a size distribution between 5 and 10 nm. Therefore, as mentioned previously, the scattered light intensity is very low and we couldn't get their correct size. Below, we show the results obtained with them. Alberto provided us a TEM (Transmission Electron Microscope) image of his particles confirming their size. The result analysis give particle sizes much above the expectations. The results are shown in Figure 35.

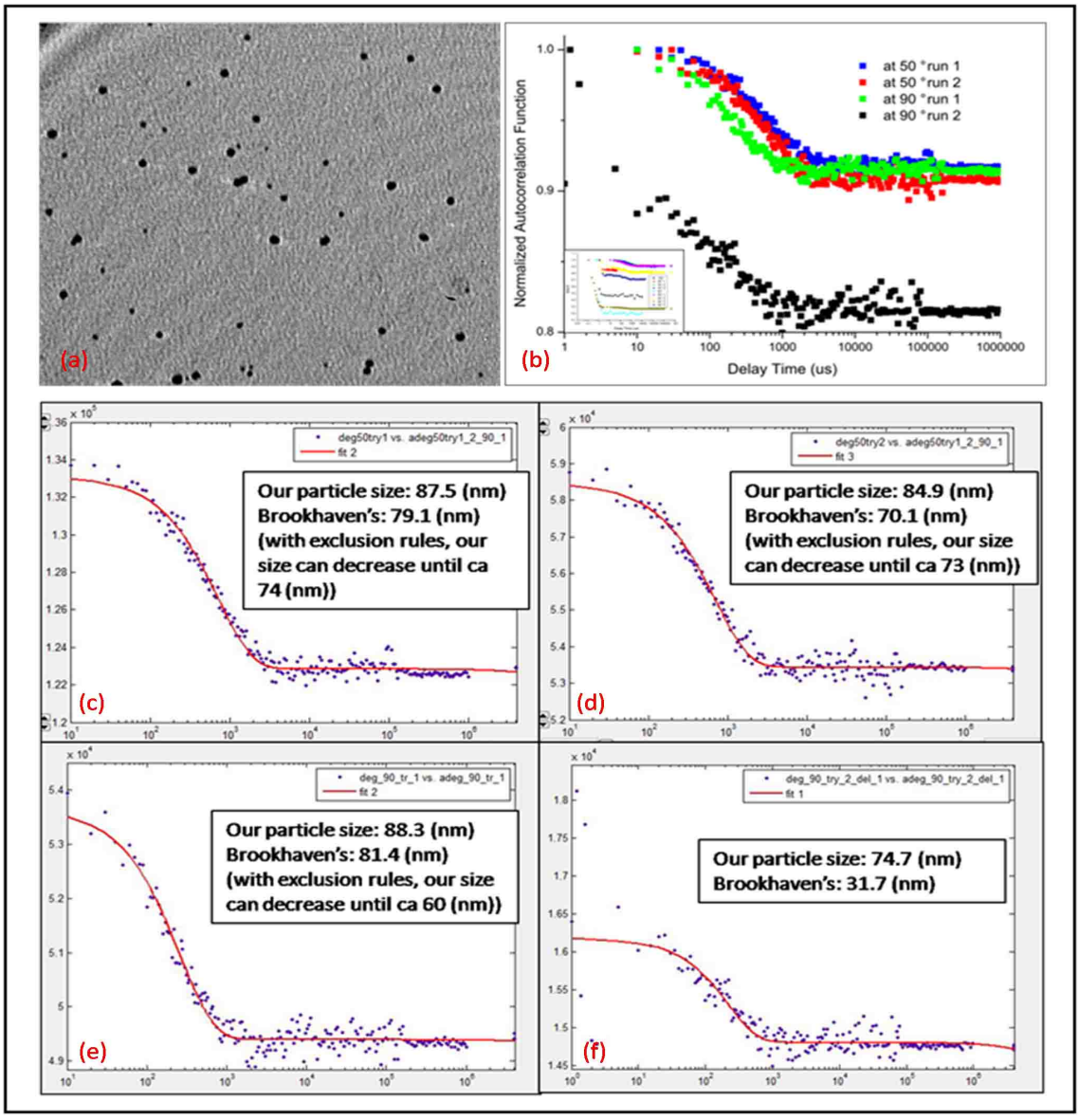

Figure 35: *AS 15 gold nanoparticles (5-10 nm in diameter). (a) TEM image showing 5-10 nm particle size. (b) Normalized ACF at 50° and 90°. (c),(d),(e) and (f) MATLAB fits with our calculated particle sizes. The results are ca. one order above the expectations. The measured signal comes probably only from additional scatterers, or nanoparticle aggregations.*

4.5 Intensity measurements varying the angle

I would like now to introduce some interesting measurements of the intensity done by varying the angle. Those measurements were done with our PS beads and with the 100 nanoparticles. The beads concentration was 0.05 % of the initial one. At this step of the project the alignment was still not perfect but we did a quick alignment of the detector optics. The measurements were taken over 30 sec for each angle. The first graph (Figure 36) is in linear scale and the second one (Figure 37) in logarithmic scale. we see that the intensity follows an exponential decay. As expected, the minimum of the intensity is at 90°, see (10).

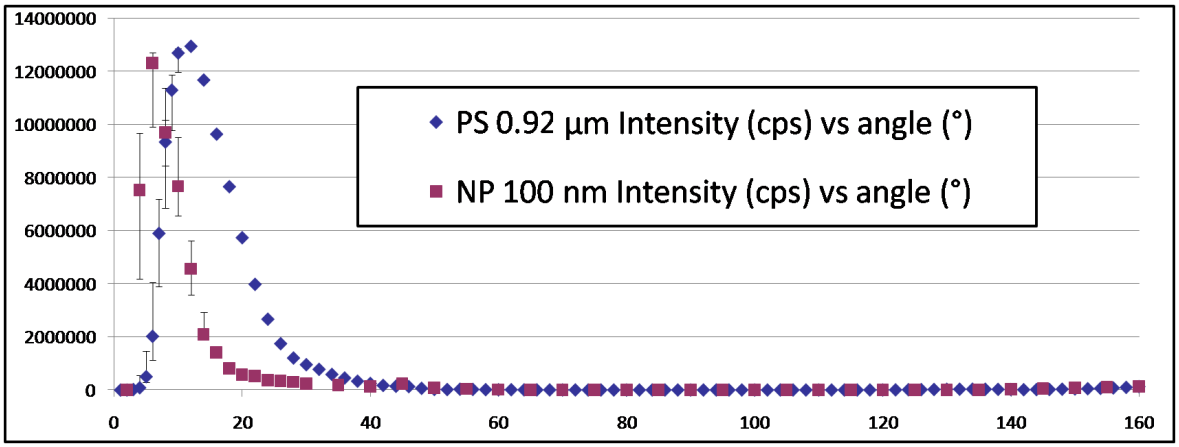

Figure 36: *Intensity measurements (angle) for PS beads and 100 nm nanoparticles in linear scale*

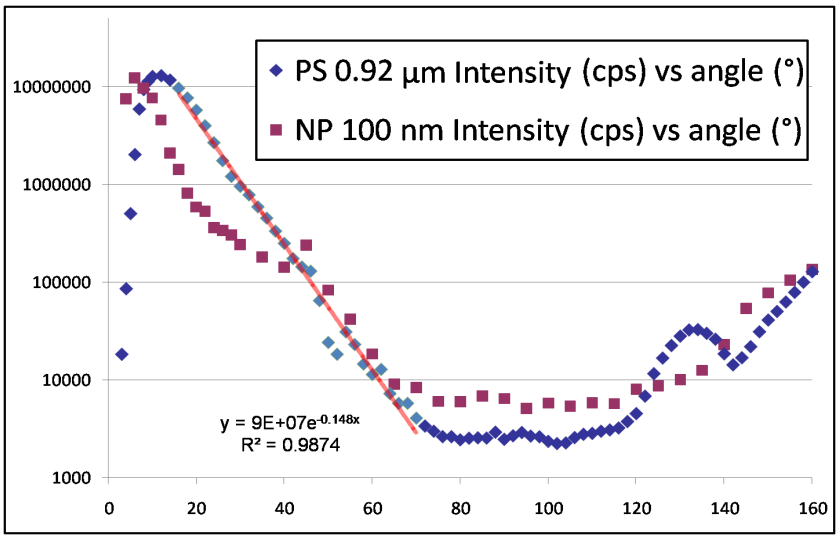

Figure 37: *Intensity measurements angle) for PS beads and 100 nm nanoparticles in logarithmic scale, the trendline is calculated by Excel for the green points*

4.6 Nanoparticles in nanopores

Since our nanopores have a diameter of 100 and 200 nanometers, it would not be possible to study particles which have a diameter in the same range. Therefore, we have acquired nanoparticles, which have a diameter of 6 nanometers. Unfortunately, as mentioned previously, the scattering intensity from these small particles turned out to be too weak to provide a reproducible autocorrelation function. The other problem that we encountered was to come up with an effective delivery method for placing the particles inside the nanopores. I describe now the various methods that we tried to insert the nanoparticles in the nanopores. We tried them with the 6 nm and also the 20 nm nanoparticles, since we could get enough intensity from the latter to study the diffusion coefficient. [3, 25, 26]

1. Putting several droplets on the membrane surface

The idea is to put one droplet on the membrane surface and to wait until it evaporates and penetrates a short distance in the nanopores. Then this process is repeated several time, until the particles are deep enough in the nanopores for confinement studies. This method was used in previous studies done with x-ray scattering and worked well.

2. Sonication of the membrane being in the nanoparticle solution

An other method which worked in other situations is to bath the membrane in the nanoparticle solution and to sonicate it during several hours. This method did not result in high enough concentrations of nanoparticles to produce strong enough light scattering intensity for DLS studies. Additional problem with this technique is that oxide membranes are fragile and can easily break during sonication process.

3. Droplets on the membrane surface with water vapor

In this approach we tried to have a persistent flow of solution vapor going through the membrane pores. Using a standard heater to produce vapor of distilled water, we add our membrane with the droplets on the top of the holder. Figure 38 shows this setup. This technique may have achieved the desired goal, since measurements of samples produced by this method resulted in measurable autocorrelation function with a much slower decay than for nanoparticles in the bulk solvent - qualitatively similar to what we would expect for nanoconfined particles.

In the Figure 39, I show some ACF obtained with this method with 20 nm gold nanoparticles and 200 nm nanopores. We see a very slow dynamics. A lot of parameters have to be taken into account before to be able to speak about the diffusion rate or related quantity of interest. Those results are still very interesting, because they appeared when the droplet was already evaporated. Even though at this large time scale a lack of coherence coming from other source

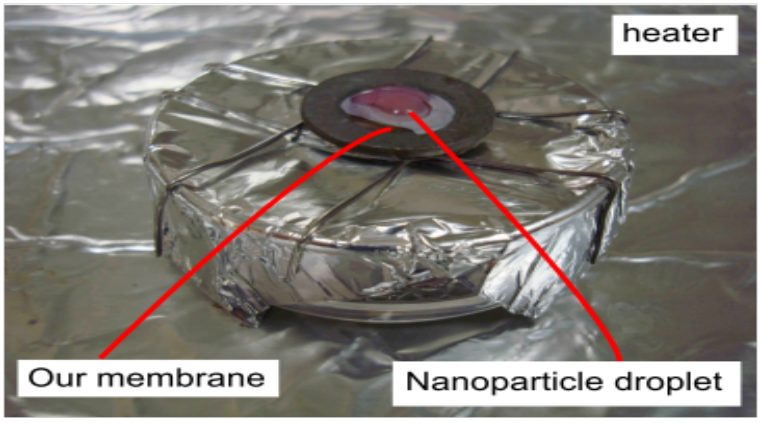

Figure 38: *The method used to insert the 20 nm nanoparticles in the nanopores. The water was heated until ca 100 °C. We add several droplets on the membrane surface.*

cannot be excluded, we can still assume that we are measuring a slower dynamics due to the particle confinement. The decay time range is still changing a lot for various experiments so, we do not show it, but it is at time range 10^2 to 10^4 times larger. This preliminary result indicates that perhaps the DLS can be in the future successfully applied to studies of nanoparticle diffusion within nanoscale confinement, using the vapor-flow-based sample synthesis technique described above.

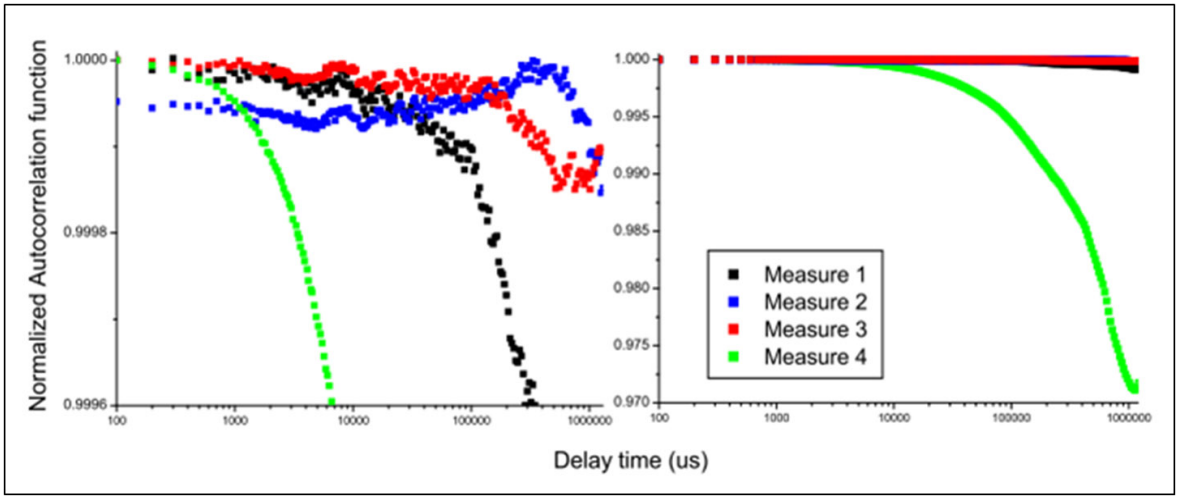

Figure 39: *Normalized ACF for confined 20 nm nanoparticles in 200 nm nanopores. We see a decay (very small) appearing at much larger time scale than in the bulk geometry.*

4.7 CCD camera - Time-varying (non-equilibrium) dynamics study

Another possibility to study the particle dynamics is to use the speckle visibility, using the process described in section 2.5. We applied this process (eq. 27) to images taken with the CCD camera. We show the results in Figure 40 for three representative images (each image represents a time series of 1D line scan speckle patterns). The time delay between each line of the image is 10 μs so that, the 2000 lines shown in Figure 40, insets (a), (b) and (c) represent a duration of 20 ms.

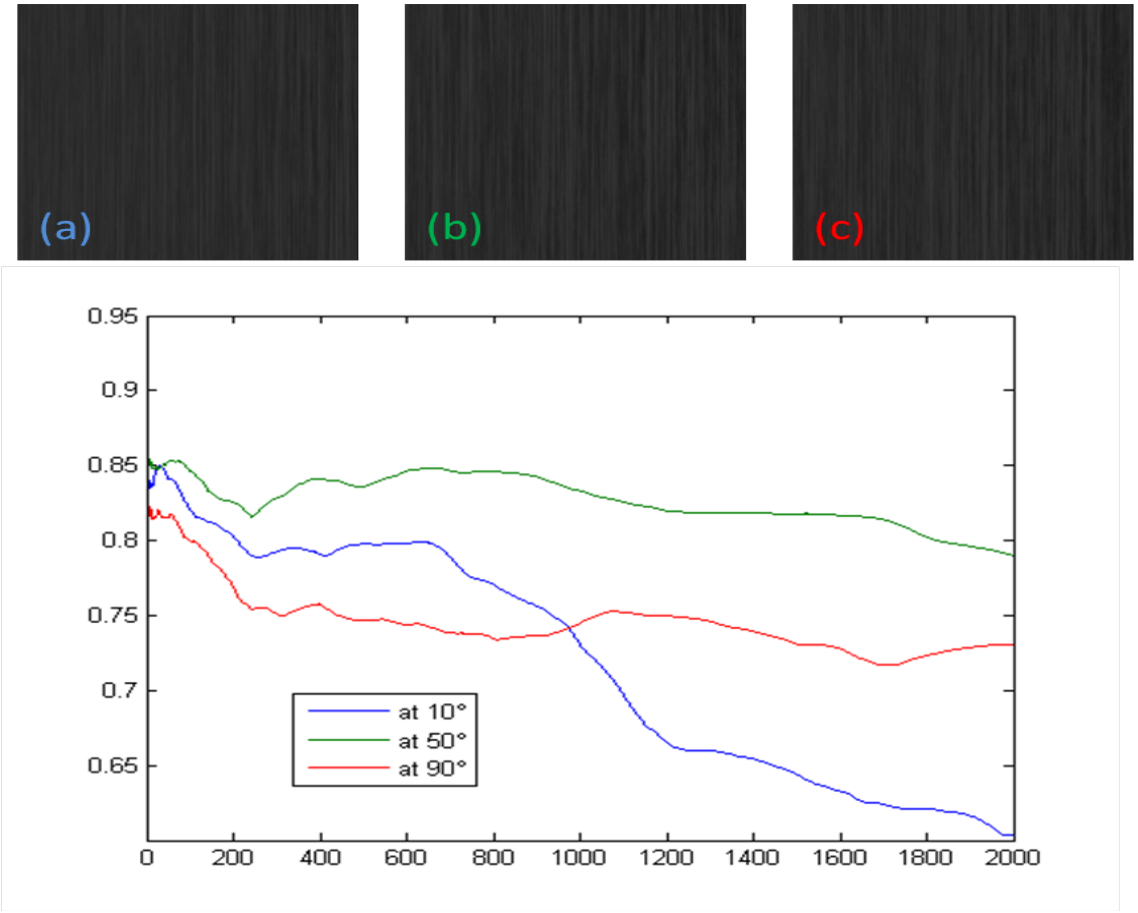

Figure 40: *CCD images and speckle visibility study of PS microbeads, at 10° (blue), 50° (green) and 90° (red). The plots show $f(\tau)$ (see Eq. 27) versus the number of lines over which is done the average. The time at which appears the decay provides us about the speckle diffusion rate.*

We see that the decays are similar for the average done over the first lines and differ substantially for more averaged lines. The time duration covered by the image (20 ms) is still an issue. To increase this duration, one possibility is to take a movie, which would provide much more than 2000 lines, therefore a longer duration, allowing studies of slower dynamics, or time-varying dynamics over a longer period of time.

4.8 X-ray Photon Correlation Spectroscopy (XPCS) data analysis

In this section I will discuss the X-ray Photon Correlation Spectroscopy (XPCS) measurements of the diffusion of nanoparticles in confinement. XPCS is in many ways analogous to DLS, but as the name implies, carried out using x-ray photons, rather than visible light.

The XPCS data presented in this thesis were collected by *Yeling Dai*, *Dr.Jioty Mohanti* and *Prof. Oleg Shpyrko* at the *Argonne National Laboratory*. The XPCS analysis program done by *Zhang Jiang* was used to generate images of the measured area and to calculate and plot the intensity vs the time and vs q, the autocorrelation functions, the contrast, the baseline and the decay time versus q. Our task consists in choosing, before the computation, the appropriate partitions, the area (mask) and the number of frames to analyze, in order to improve the correlation function accuracy and obtain the expected q dependence. The choice of the partition number, which determines the number of points (areas) which are correlated can improve the statistics and therefore the correlation function accuracy. To get accurate results we would like the intensity being constant over all the frames that we use in auto-correlation function calculations. Since the intensity has the tendency of decreasing with the time, possibly due to beam damage effects, we have removed the frames that show substantial drop in total recorded intensity, limiting the autocorrelation function to the frames which exhibit roughly similar values of total intensity, as shown in Figure 41. As the Figure 41, inset (a) shows, the onset of x-ray induced damage begins to become noticeable (loss of approximately 1-2 % of scattered intensity) after 200 to 300 seconds of x-ray exposure. As the examples in insets (c) and (d) of Figure 41 demonstrate, limiting the data analysis to the first 100 frames produces autocorrelation function with a considerably shorter characteristic decay timescale, as opposed to the same calculations performed for the entire dataset, which tend to pick up the long-term beam-damage loss of intensity and extend the characteristic time constants to that associated with the beam damage effects.

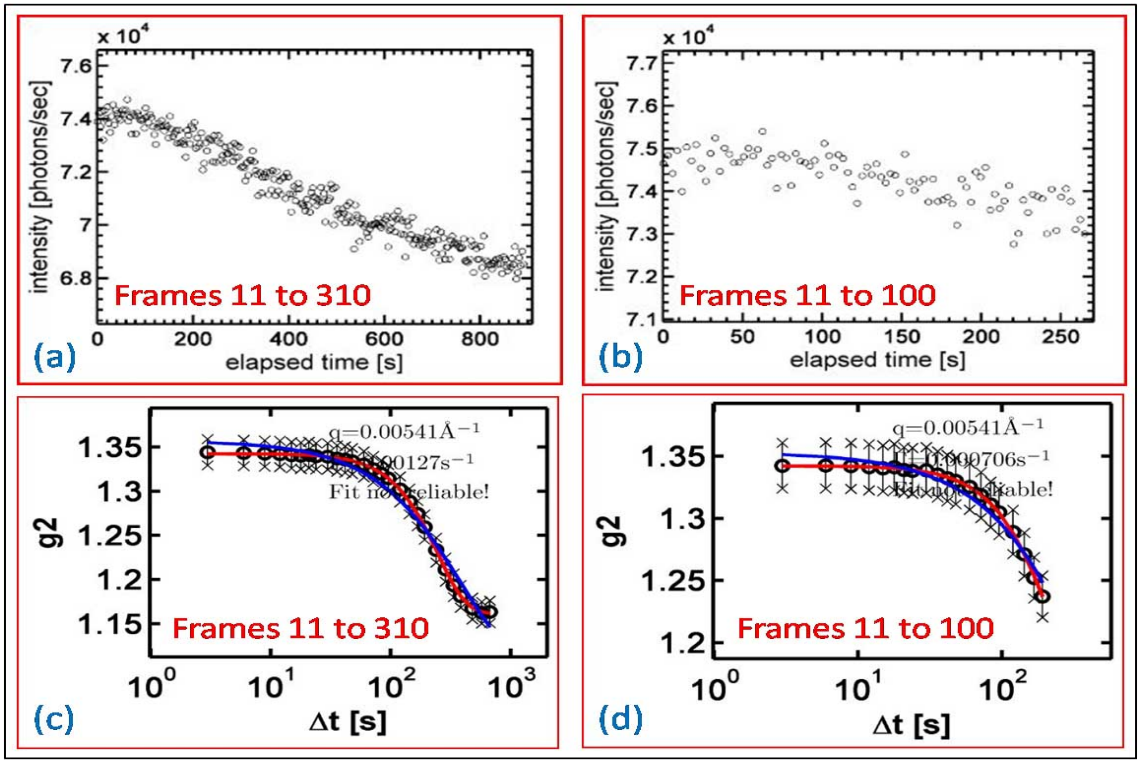

Figure 41: *(a) and (b) The drop in the intensity is taken off before correlation by taking off a part of the frames off the XPCS measurements. (c) and (d) As a consequence, the corresponding correlation time range is shortened.*

5 Discussion

Since our project is in its early developmental stages, we invested a substantial amount of time to the understanding of the different challenges of DLS.

5.1 First steps

A simple DLS experiment with large scatterers could be very successful and give the idea of a simple analyze method. As an example, even with standard milk, we easily autocorrelation functions, featuring decay times within the expected range. The time of the decay was in a reasonable range. In contrast, the DLS experiments on very small (nanometer) scale particles present a number of technical and experimental challenges.

The choice of an appropriate solution container presented one of the first encountered challenges. The thin capillaries have the disadvantage that the light is reflected on the edge of the capillary producing a very bright line, severely complicating the scattering contributions from the solvent. Even though the strong contribution from internal reflection can be redirected if the capillary is used in a different orientation, for example horizontally, the disadvantage of this solution is the loss of cylindrical symmetry that comes with it.

We also tried our experiments with the solution being "sandwiched" between two coverslips. This configuration has the advantage that the coverslips are optically "cleaner" than the pyrex tubes, but again, the lost of the center of rotation and of the cylindrical symmetry is an important disadvantage.

Another option is to use pyrex tubes. More solution is required to reach the appropriate height of solution in the tube. The pyrex tubes appear not as precisely manufactured as the thin capillaries. On the positive side, since the tubes are made of pyrex, their refractive index is very close to the one of our matching solution and the vat. Pyrex tubes turn out to be the more appropriate containers for our experiments.

After the alignment of the DLS setup, we saw a great improvement in the intensity of the incident light (little or no stray scattering from empty container), giving us more accurate results. Measuring a high intensity has several advantages. One is that the sample concentration can be reduced decreasing the multiple scattering. Another one is the possibility of using a smaller pinhole resulting in higher degree of coherence (Siegert coefficient). In the case of small nanoparticles, in order to measure scattered intensity signal, a high incident intensity is required, since the interaction of the laser light with the particles is already week.

5.2 Polystyrene (PS) microbeads

The beads, having a size close to 1 μm, with our 633 nm wavelength laser, give us a strong signal and therefore nice correlation functions. We could obtain the q dependence of the time decay.

5.3 "Large" gold nanoparticles

I call "Large" nanoparticles, the 100, 50 and 20 nm (diameter) gold nanoparticles. In contrast to the "Small" ones, the 6 nm and the AS 15 5-10 nm (diameter), the "Large" nanoparticles are enough big to be analyzed with our experimental setup. In fact, since the scattered intensity for a single scatter depends on the radius at the power of 6, a particle with a 10 times smaller radius will scatter 1 million time less. This is the principle reason making the DLS analysis of small nanoparticles with a 633 nm wavelength laser is so difficult. It is not easy to obtain enough intensity and accurate ACF from the 20 and 50 nm nanoparticles. This difficulty is not only due to the laser but also to the sample preparation. Standard water, being not filtered, has usually a lot of particles or compounds with a size comparable or even bigger than the particles of interest. As a consequence the light is not only scattered from our nanoparticles but also from those unwanted scatterers. Even a single event from a large unwanted compound will have a much stronger influence in the results than the large amount of scattering from nanoparticles. It is therefore very important to make the samples with filtered water or even distilled one.

For the 20 nm gold nanoparticles, the results are not very accurate. The reason is that the filter, from the water purificator, have a pore size of ca. 200 nm, which means that they are not able to filter compounds which are much bigger than our 20 nm nanoparticles. In the results, shown in the Figure 31, we see clearly the peaks in the intensity coming from those compounds. It is therefore required to use distilled water for the sample preparation.

5.4 "Small" gold nanoparticles

As mentioned above, in the "small" nanoparticles, I include the 6 nm gold nanoparticles and the 5-10 nm AS 15 gold nanoparticles. The scattering intensity from these small particles turned out, after several experiments in various conditions, to be too weak to measure obtain reasonable ACF. The intensity dependence of the scattered light in the particle size, discussed in the section 2.5 is the main reason. Since an adequate intensity for, as an example 50 nanometer nanoparticles, is 500 kcps, and with the relation introduced in chapter 2.5, we see that a diameter ratio of 10 will give an intensity ratio of 1,000,000, giving an intensity in the order of 0.5 cps (far too low to be detected). At that size, an other problem, even with distilled water is that all containers should be extremely clean. Any additional compound, larger than

6 nm will play a huge role.

Since it is always good to have a comparison between different kinds of samples, it was interesting to measure the AS 15 gold nanoparticles. They have a diameter between 5 and 10 nm thus we can expect the same problem than with the 6 nm gold nanoparticles. We worked in "clean" conditions, using high quality distilled water and clean tools and containers. We tried several concentrations, at several angles, with different pinhole sizes but we couldn't obtain reproducible quality results. Figure 10 shows measurements at large angles. The measured particle size is much larger than expected. The advantages of large angles is that the unwanted larger scatterers and multiple scattering have a smaller impact. The much larger measured sizes than expected cannot be precisely explained. It is possible that the particles tend to agglomerate and thus we get signal not from a single particle, but from a kind of "big blob" of particles. Another possibility is that even with a serious cleaning procedure, we still had some extra compounds. Finally, especially because of the reproducible obtained results, we cannot exclude that the hydrodynamic diameter is much larger than the "naked" gold particles. In that fact, we could obtain the information about the particle sizes with the ligands.

A way to increase the intensity is to work with higher concentration. We have, in that case, more scattering, which yields to a higher scattered intensity. But increasing the concentration will also increase multiple scattering, which has the effect of lowering the measured particle size. In order to get very accurate particle sizing, an appropriate angle has to be chosen. Theoretically, the concentration shouldn't play a so important role, but experimentally, it is still better to stay in a range that can be preliminarily determined.

To conclude with "small" nanoparticles, we are in front of a serious compromise, either working at high angles and therefore avoid to much contribution from extra compounds and multiple scattering, or working at small angles and having a higher intensity. In any case, a laser with a shorter wavelength seems necessary to study this particle size range.

5.5 DLS - The Challenge

The DLS experiment is often presented as a very simple and trivial method for characterization of particle sizes - and often used by biologists and chemists in "black box" mode, without paying significant attention to experimental artifacts encountered by us and described in detail in this thesis. In fact, even though it is possible to produce an analyze setup and calibrate it in a way to avoid all experimental difficulties, as an example a lot of those setups have been produced for particle sizing, a complete understanding and accurate use of this method is far more challenging.

In the previous sections, the results of each step of our project have been systematically analyzed. In the present chapter, I would like to go beyond those steps, and list the main

difficulties that we had to solve during this work. With a more general point of view, those considerations are also the main ones that should be taken into account in every DLS experiment. I present them, starting from the easiest to solve to the most challenging one.

1. The Alignment

The alignment is a long but important step. The two main reasons are the angle (q) dependence and the intensity of the measured light. If the scattering occurs out of the rotation center, the angle dependence is lost. If the light which reach the detector is has a low intensity, it particle size range will be limited, since the light scattered from particles with a diameter much smaller than the laser wavelength is already low (13).

2. Scattering on container walls

When the laser beam reaches the surface of a new media having a higher refractive index, it is reflected. As a consequence, additionally to the light scattered from the sample, our detector measures the light reflected from the sample container. As mentioned in section 2.6, in an Homodyne experiment, making the assumption that our signal comes only from the scattered light, we do not want to have any contribution from a local oscillator. Otherwise we should involve the Heterodyne autocorrelation function. To avoid this unwanted phenomena, it is very important that the change (from small to greater) in the refractive index occurs far from our sample. This imply a careful choose in the of the sample container. In this purpose, the vat and its matching index solution can help, as described in section 3.1.

3. The Polydispersity

In the purpose of correct results, it is very important to have monodisperse particle size. It came out during our work that large components scatter the light much more than small ones. Therefore, unwanted very large components will play a huge rule in the results despite they scatter the light much more rarely than the particles under study. It is expressed by the relation (13) and shown in 31. As a consequence the purity of the water used to make solutions of small particles is extremely important.

4. Multiple scattering

The multiple scattering remains a real challenge. Even though physicists found methods to suppress it, with our setup we couldn't, for the moment, involve such methods. In the calculation, it is supposed that the photon undergo only one interaction before to reach the detector and that the latter occurs at the center of rotation . In the case of multiple scattering, this not the case any more. The angle (q) dependence is lost. As seen during our work, the concentration and the scattering volume of the sample pays a role. The photon free path is

determined by the concentration but should also not be much shorter than the volume typical length.

As a consequence of the previous discussion, one important remaining challenge in our setup, is to avoid multiple scattering and simultaneously reflection of the light from the container wall. In this view, and thinking about the measured intensity, the choices of an appropriate concentration and angle of experiment are crucial and tricky decisions.

5.6 CCD Camera - Speckle size

With the preliminary result shown in Figure 40, we show that the method discussed in section 2.5 is feasible. At this stage, accurate results and a complete understanding still require a lot of investments. A very interesting issue is to compare the dynamics obtained with this process and the one obtained with a usual intensity correlation, measured either with a DLS setup or with a CCD camera. The possibility to study time varying (non-equilibrium) dynamics opens the way for a large range of new studies, for our nanoparticles as well as for a multitude of other systems. [12]

As a consequence, dynamics studies involving both DLS and XPCS has a long future. The interest arises from the complementarity of the information provided by those methods.

6 Conclusion

As often happens in scientific research, it is difficult to predict the complex path on which science takes us well ahead of time. In this context, the original title of my master thesis should be taken rather generally, as the scope of research presented here has been primarily focusing on fundamental aspects of diffusion of micro- and nanoscale particles in confined geometries. Nevertheless, it is important to underscore that understanding of many aspects of dynamic light scattering measurements thoroughly investigated and presented here is crucial as the basis for future work to be performed on more complex systems. As this thesis illustrates, Dynamic Light Scattering setup can by means be considered a simple "black box" system that can be used to obtain reliable particle sizing results without thorough understanding of underlying physical processes.

In this thesis I demonstrated that Dynamic Light Scattering can be an effective tool in probing diffusion of particles with sizes ranging from micron-scale down to a few nanometers, even though there are many experimental precautions that need to be undertaken for the DLS experiments to be successful for particle sizing in nanometer-scale range. We have also contrasted traditional DLS measurements with a multi-speckle DLS approach, particularly useful in studies of non-equilibrium processes.

Having learnt about and obtained satisfactory results with our DLS setup, installed the CCD camera on the DLS setup, introduced several dynamic study methods and apparently found out a method to insert the nanoparticles in nanopores, the approach to diffusion coefficient studies with interesting information is now possible. The DLS allows fast dynamic studies and in an other hand the CCD camera offer the possibility of better statistics for slower dynamics. Having two methods for particle dynamics studies, a very interesting orientation will be to compare the results that can be provided by both.

7 List of figures

List of Figures

Bibliography

References

[1] David J Beebe, Glennys A Mensing, and Glenn M Walker. Physics and applications of microfluidics in biology. *Annual Review of Biomedical Engineering*, 4:261–86, 2002. PMID: 12117759.

[2] Carl Hansen and Stephen R Quake. Microfluidics in structural biology: smaller, faster... better. *Current Opinion in Structural Biology*, 13(5):538–544, October 2003.

[3] K. J Alvine, O. G Shpyrko, P. S Pershan, K. Shin, and T. P Russell. Capillary filling of anodized alumina nanopore arrays. *cond-mat/0612119*, December 2006. Phys. Rev. Lett. 97, 175503 (2006).

[4] S. B. Dierker, R. Pindak, R. M. Fleming, I. K. Robinson, and L. Berman. X-Ray photon correlation spectroscopy study of brownian motion of gold colloids in glycerol. *Physical Review Letters*, 75(3):449, 1995. Copyright (C) 2009 The American Physical Society; Please report any problems to prolaaps.org.

[5] Robert Brown. A brief account of microscopical observations. In John J. Bennett, editor, *Edinburgh new Philosophical Journal*, pages 358–371. July - September 1828.

[6] Albert Einstein. Uber die von der molekularkinetischen theorie der warme geforderte bewegung von in ruhenden flussigkeiten suspendierten teilchen. *Annalen der Physik*, pages 549 – 560, May 1905.

[7] Marian Smoluchowski. Zur kinetischen theorie der brownschen molekularbewegung und der suspensionen. *Annalen der Physik*, pages 756 – 780, July 1906.

[8] Hendrik Christoffel Hulst. *Light Scattering by Small Particles*. 1981.

[9] Andreas P. Fr?oba, Stefan Will, and Alfred Leipertz. Light scattering by surface waves on a vertical layer of liquid toluene. *Applied Optics*, 36(30):7615–7620, October 1997.

[10] Luca Cipelletti and D. A. Weitz. Ultralow-angle dynamic light scattering with a charge coupled device camera based multispeckle, multitau correlator. *Review of Scientific Instruments*, 70(8):3214–3221, 1999.

[11] Bruce J. Berne and Robert Pecora. *Dynamic Light Scattering*. 2000.

[12] R. Bandyopadhyay, A. S. Gittings, S. S. Suh, P. K. Dixon, and D. J. Durian. Speckle-visibility spectroscopy: A tool to study time-varying dynamics. *Review of Scientific Instruments*, 76(9):093110–11, 2005.

[13] Pavel Zakharov, Suresh Bhat, Peter Schurtenberger, and Frank Scheffold. Multiple-scattering suppression in dynamic light scattering based on a digital camera detection scheme. *Applied Optics*, 45(8):1756–1764, March 2006.

[14] Jr. Charles S. Johnson and Don A. Gabriel. *Laser Light Scattering*. 1981.

[15] Zhang Jiang. *X-ray Scattering Studies of Structure and Dynamics of Surfaces and Interfaces of Polymeric Liquids*. PhD thesis, University of California, San Diego, 2007.

[16] Eric Dufresne. *Intensity fluctuation spectroscopy with coherent X-rays*. PhD thesis, McGill University, Montreal, Canada, 1995.

[17] F. Scheffold and R. Cerbino. New trends in light scattering. *Current Opinion in Colloid & Interface Science*, 12(1):50–57, February 2007.

[18] Klaus Schaetzel. Suppression of multiple scattering by photon cross-correlation techniques. *Journal of Modern Optics*, 38(9):1849–1865, 1991.

[19] S. Kirsch, V. Frenz, W. Schartl, E. Bartsch, and H. Sillescu. Multispeckle autocorrelation spectroscopy and its application to the investigation of ultraslow dynamical processes. *The Journal of Chemical Physics*, 104(4):1758–1761, 1996.

[20] Gerhard Gruebel and Federico Zontone. Correlation spectroscopy with coherent x-rays. *Journal of Alloys and Compounds*, 362(1-2):3–11, 2004.

[21] Brookhaven Instruments Corporation, 750 Blue Point Road, Holtsville, New York 11742, U.S.A. *Instruction Manual for BI-9000AT Digital Autocorrelator*, 1.0 edition, May 1998.

[22] C. N. Ramachandra Rao, Giridhar U. Kulkarni, P. John Thomas, and Peter P. Edwards. Metal nanoparticles and their assemblies. *Chemical Society Reviews*, 29(1):27–35, 2000.

[23] O Jessensky, F Muller, and U Gosele. Self-organized formation of hexagonal pore arrays in anodic alumina. *Applied Physics Letters*, 72(10):1175, 1173, 1998.

[24] Hideki Masuda and Kenji Fukuda. Ordered metal nanohole arrays made by a Two-Step replication of honeycomb structures of anodic alumina. *Science (New York, N.Y.)*, 268(5216):1466–1468, June 1995. PMID: 17843666.

[25] C. Jeffrey Brinker, Yunfeng Lu, Alan Sellinger, and Hongyou Fan. Evaporation-Induced Self-Assembly: nanostructures made easy. *Advanced Materials*, 11(7):579–585, 1999.

[26] Eran Rabani, David R. Reichman, Phillip L. Geissler, and Louis E. Brus. Drying-mediated self-assembly of nanoparticles. *Nature*, 426(6964):271–274, November 2003.

Appendix

A.1 X-Ray Photon Correlation Spectroscopy

In this section, I show one complete set of XPCS information provided by the program done by *Zhang Jiang*, as used in in section 4.8. For this set, the pores are 200 nm and the particles 5 nm (in diameter). Glycerol was added in the solution in the purpose of a slower dynamics (higher viscosity). In the Figure 42, we see the intensity measured by each pixel as well as versus the time. We see in the Figure 42 that the intensity is not stable over the time, as discussed in the chapter 4.8. We also see that the intensity is higher by large column and row number. In the Figure 43, as expected, we see that the intensity decreases while the q value increases. This is the reason why, in the Figure 44 and in the Figure 45, the correlation functions become unclear as q increases (too low intensity). In the next images, Figures 46, 47 and 48, various parameters are provided, such as the contrast (a higher contrast yields greater decays in the correlation function), the baseline (normalization factor) and the decay time, τ (expected to be constant).

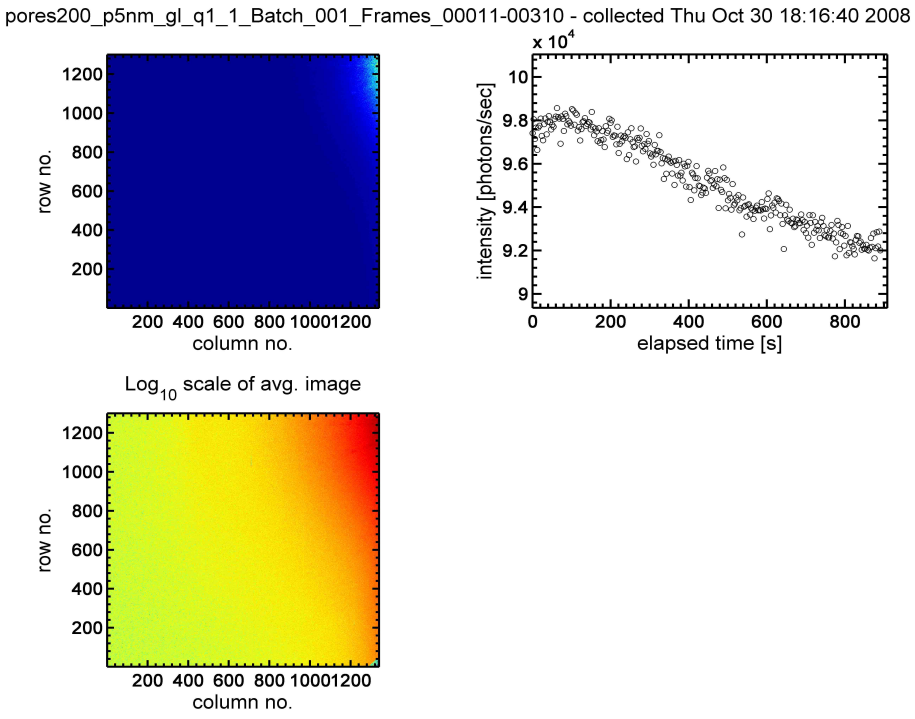

Figure 42: *XPCS data, Intensity vs time and pixel.*

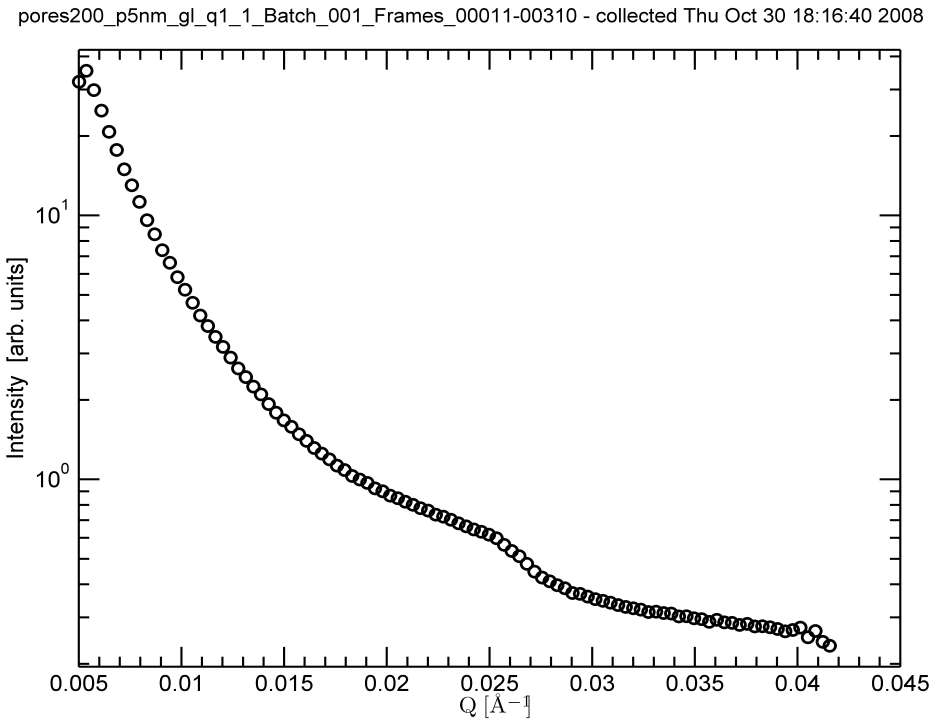

Figure 43: *XPCS data, Intensity vs time*

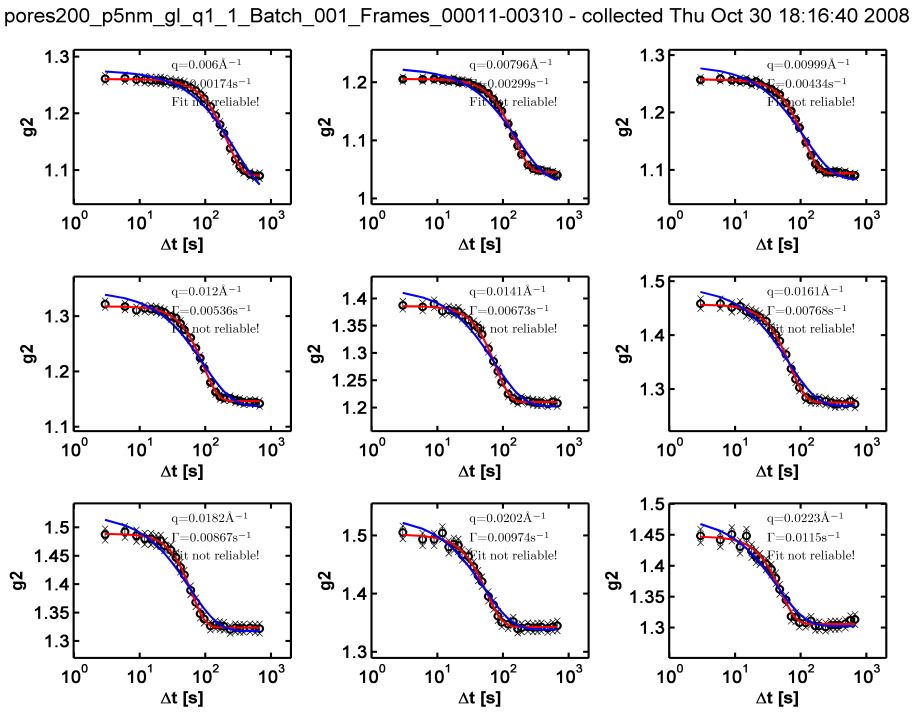

Figure 44: *XPCS data, Correlation functions for various q*

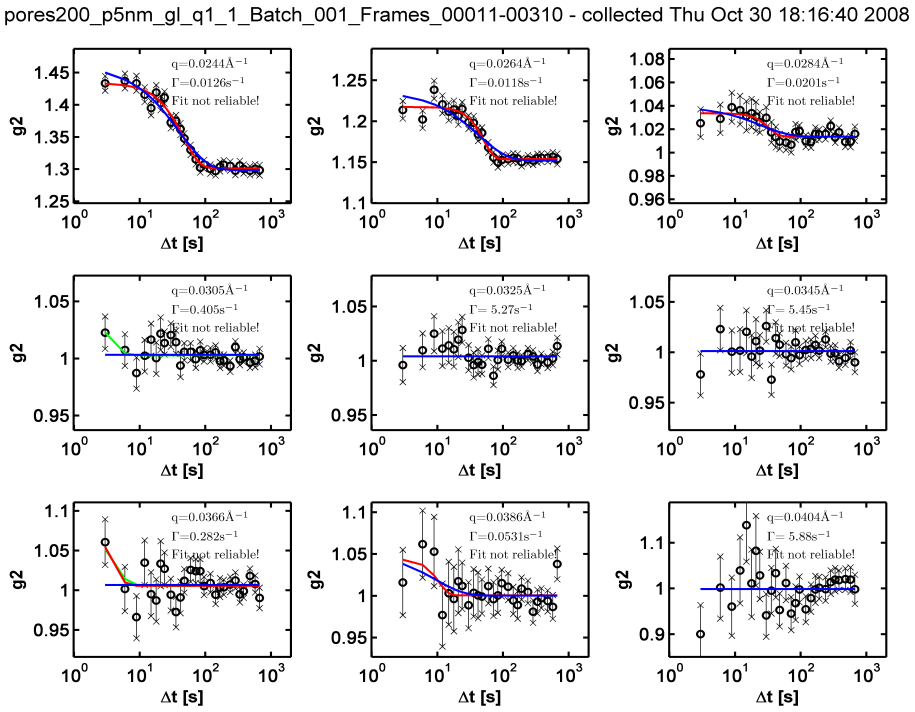

Figure 45: *XPCS data, Correlation functions for various q*

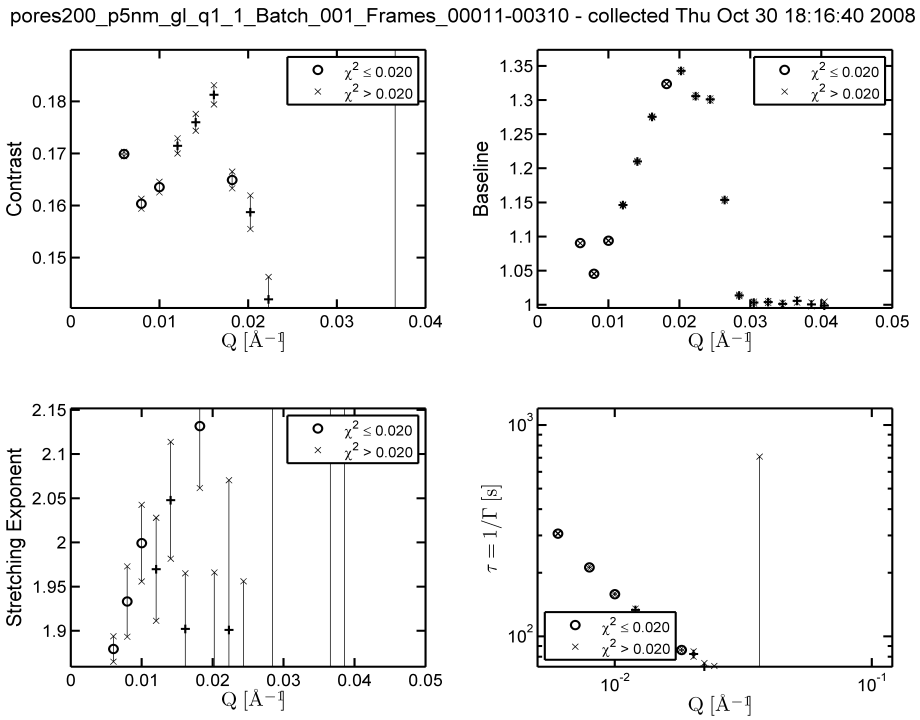

Figure 46: *XPCS data, Various parameters*

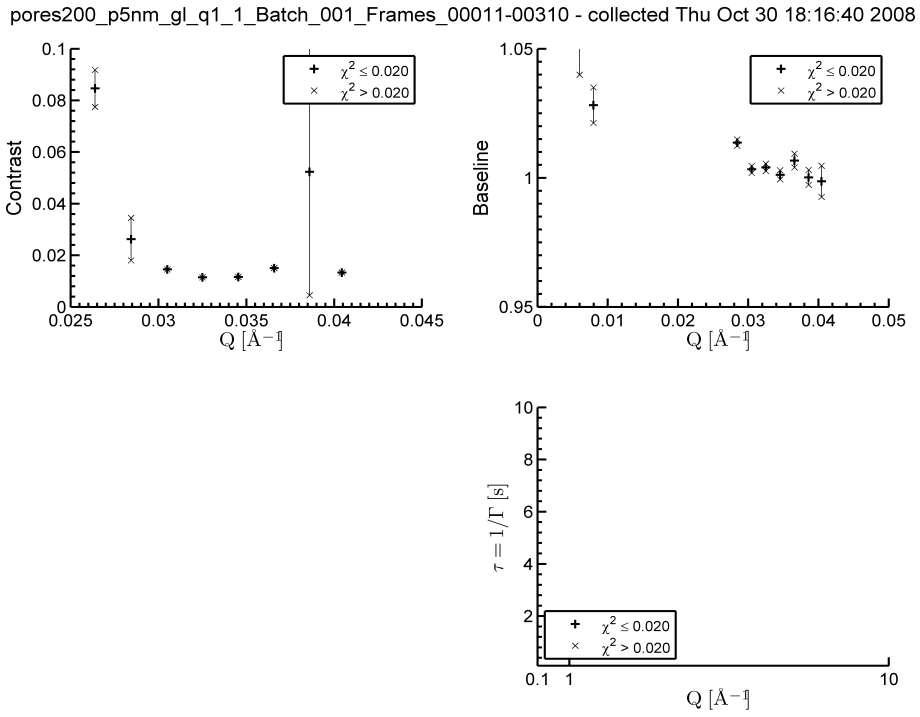

Figure 47: *XPCS data, Various parameters*

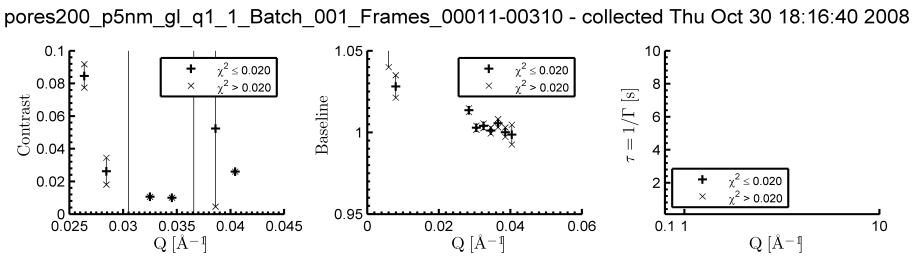

Figure 48: *XPCS data, Various parameters*